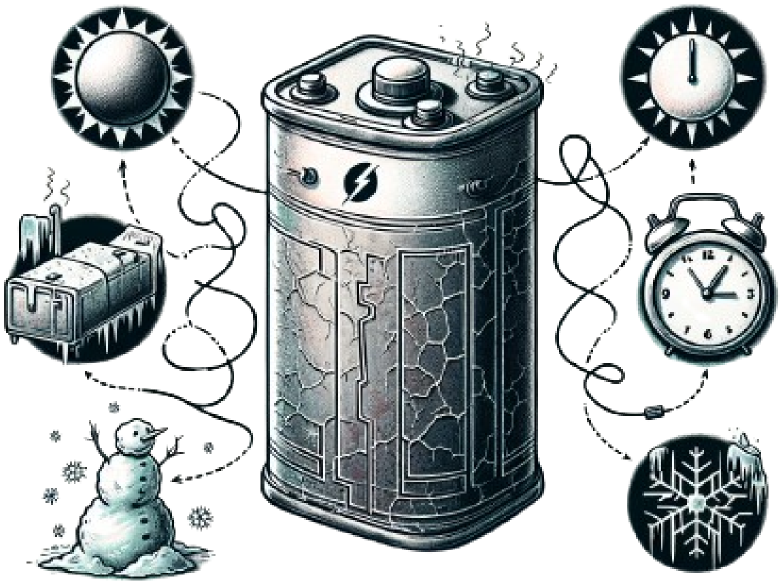

Estimation of Degradation Modes for Lithium-ion Batteries

Estimation of degradation modes of an aged battery using Open-Circuit Voltage curves

Master's thesis in System, Control and Mechatronics

MUKUNDH BALABHADRA
YOGITH MADHA

DEPARTMENT OF ELECTRICAL ENGINEERING

CHALMERS UNIVERSITY OF TECHNOLOGY
Gothenburg, Sweden 2024
www.chalmers.se

Master's thesis 2024

Estimation of Degradation Modes for Lithium-ion Batteries

Estimation of degradation modes of an aged battery using Open-Circuit Voltage curves

MUKUNDH BALABHADRA
YOGITH MADHA

Department of Electrical Engineering
Division of Systems, Control and Mechatronics
Chalmers University of Technology
Gothenburg, Sweden 2024

Estimation of Degradation Modes for Lithium-ion Batteries
Estimation of degradation modes of an aged battery using Open-Circuit Voltage curves
MUKUNDH BALABHADRA
YOGITH MADHA

Supervisor: Björn Fridholm, Technical Expert Traction Battery Controls at Volvo Cars
Examiner: Torsten Wik, Professor, Chalmers University of Technology

Master’s Thesis 2024
Department of Electrical Engineering
Division of Division name
Chalmers University of Technology
SE-412 96 Gothenburg
Telephone +46 31 772 1000

Cover: Visualization of various aging/degradation parameters on batteries.
https://www.monolithai.com/blog/battery-aging

Typeset in LaTeX
Printed by Chalmers Reproservice
Gothenburg, Sweden 2024

Estimation of Degradation Modes for Lithium-ion Batteries
Estimation of degradation modes of an aged battery using Open-Circuit Voltage curves
MUKUNDH BALABHADRA
YOGITH MADHA
Department of Electrical Engineering
Chalmers University of Technology

Abstract

Lithium-ion batteries (LIB) have become essential in the automotive industry due to their favorable properties of high volumetric and weight-based energy density, low self-discharge rates, and relatively affordable costs. Due to their widespread use, comprehending the life cycle dynamics of LIB is paramount. Over time, the internal chemistry of these batteries undergoes changes, leading to variations in power and capacity output, commonly referred to as power and capacity fade. Accurate prediction of end-of-life (EoL) is pivotal as it allows for the mitigation of accelerated degradation risks, thereby Improving operational lifespan.

The present study endeavors to analyze and develop a non-destructive methodology for estimating the degradation modes of LIBs, utilizing both pristine and aged Open-Circuit Voltage (OCV) curves. The primary objective is to devise methodologies that can estimate the degradation mode to high accuracy given the batteries' OCV. The ultimate goal is to establish techniques for estimating degradation modes within LIBs on an online platform, thus facilitating a better understanding of battery degradation processes. By quantifying the extent of aging within the battery, this approach aims to empower Battery Management Systems (BMS) to proactively adapt and optimize operational strategies, consequently prolonging the lifespan of battery packs deployed in vehicles.

This dissertation presents findings that compare experimental results with simulations conducted using PyBaMM. The experiments are conducted under diverse circumstances mirroring real-world scenarios, encompassing considerations such as down-sampled data points, sensor noise, and data segmentation. Through this comprehensive investigation, this research contributes to advancing the understanding of LIB degradation dynamics and lays a foundation for the development of robust predictive maintenance strategies for traction batteries in automotive applications.

Keywords: lithium-ion, Open-Circuit Voltage (OCV) curve, degradation modes, open-circuit potential, optimization.

Acknowledgements

We extend our sincere gratitude to our esteemed tutors, Björn Fridholm, Fredrik Bengtsson, and Marcus Hedegärd, whose guidance, support, and collaborative demeanor were indispensable throughout our academic pursuit. Their continuous assistance and invaluable insights played an integral role in shaping the outcome of our research endeavors. Special acknowledgment is extended to Velibor Djordjic for his prompt assistance during the setup process, and to Volvo Car Corporation for providing the opportunity to work on batteries and software.

We also express our sincere appreciation to Prof. Torsten Wik at Chalmers University, our esteemed examiner, for his invaluable guidance and scholarly input, which significantly enriched the quality of our project. We are deeply grateful for his steadfast support.

Lastly, we wish to convey our heartfelt gratitude to our families and friends. Their support and encouragement have served as a constant source of strength throughout our academic journey. Without their steadfast belief in our endeavors, this work would not have been possible.

Mukundh Balabhadra and Yogith Madha, Gothenburg, May 2024

List of Acronyms

Below is the list of acronyms that have been used throughout this thesis listed in alphabetical order:

BMS	Battery Management Systems
CV	Cyclic Voltammetry
DAEs	Differential Algebraic Equations
DFN	Doyle–Fuller–Newman Model
DRT	Distribution of Relaxation Times
DVA	Differential Voltage Analysis
ECMs	Equivalent Circuit Models
EIS	Electrochemical Impedance Spectroscopy
EoL	End-of-Life
EV	Electric Vehicle
GITT	Galvanostatic Intermittent Titration Technique
HPC	High Precision Coulometry
HPPC	Hybrid Pulse Power Characterization
ICA	Incremental Capacity Analysis
LAM	Loss of Active Material
LAM_{NE}	Loss of Active Material in the Negative Electrode
LAM_{PE}	Loss of Active Material in the Positive Electrode
LCO	Lithium Cobalt Oxide
LIBs	Lithium-Ion Batteries
LFP	Lithium Iron Phosphate
LLI	Loss of Lithium Inventory
NE	Negative Electrode
NMC	Lithium Nickel Manganese Cobalt Oxide
OCP	Open-Circuit Potential
OCV	Open-Circuit Voltage
OEMS	Online Electrochemical Mass Spectrometry
ODEs	Ordinary Differential Equations
PBMM	Python Battery Mathematical Modelling
P2D	Pseudo-Two-Dimensional
PE	Positive Electrode
pSEI	Positive Solid Electrolyte Interface
RMSE	Root Mean Square Error
ROCV	Reconstructed Open Circuit Voltage

SEI	Solid Electrolyte Interface
SOC	State of Charge (SOC[%])
SoH	State of Health
SPM	Single Particle Model without Electrolyte
SPMe	Single Particle Model with Electrolyte
XCT	X-ray Computed Tomography

Nomenclature

Below is the nomenclature of indices, parameters, and variables that have been used throughout this thesis.

Indices

x	Index for Positive/Negative electrode.
i	Index of data.

Parameters

α	Linear scaling factor.
β	Shifting factor.
$\alpha_{PE,pris}$	Linear scaling factor for pristine cathode(Positive).
$\alpha_{NE,pris}$	Linear scaling factor for pristine anode(Negative).
$\beta_{PE,pris}$	Shifting factor for pristine cathode(Positive).
$\beta_{NE,pris}$	Shifting factor for pristine anode(Negative).
x_{PE}	Stoichiometry coefficient for cathode(Positive).
x_{NE}	Stoichiometry coefficient for anode(Negative).
C_s	Current lithium concentration in the electrode.
C_s^{max}	Maximum lithium concentration in the electrode.
U_{PE}	Voltage of positive electrode (V).
U_{NE}	Voltage of negative electrode (V).
U_{full}	Voltage of full cell (V).
t	Time (sec).
t_0	Initial time (sec).
C_n	Nominal cell capacity (A.h).
I	Current flowing in and out of the cell (A).

C_{update}	Updated cell capacity (A.h).

Variables

LLI	Degradation mode- loss of lithium inventory (%).
LAM_{PE}	Degradation mode- loss of active material in positive electrode (%).
LAM_{NE}	Degradation mode- loss of active material in negative electrode (%).
OCV_{meas}	Measured OCV curve (V).
OCV_i	Predicted OCV curve (V).
N	total number of sample points.
$\theta_{m/d}$	Optimization parameters.

Contents

List of Figures

List of Tables

1

Introduction

In the rapidly advancing field of electric vehicle (EV) technology, the intricate nature of batteries has become a central focus of exploration. Among these, lithium-ion batteries (LIBs) stand out as pivotal energy storage solutions within the automotive sector due to their high energy density. Consequently, LIBs have garnered significant attention in research efforts aimed at improving and optimizing their operational efficiency and lifespan [1].

To delve deeper into the internal dynamics of LIBs, rigorous modeling endeavors are inevitable. Within the automotive industry, the state of the art is to use Equivalent Circuit Models (ECMs) integrated within Battery Management Systems (BMS) to navigate the complexities of battery dynamics [2]. However, ECMs come with their own set of challenges, including limited explanatory power, susceptibility to operational conditions, and constraints related to spatial resolution. Currently, physics-based models stand at the forefront of these endeavors, offering comprehensive depictions of battery behavior. Despite their sophistication, the practical utility of physics-based models is impeded by computational demands, particularly concerning real-time applications in automotive systems.

With the increasing use and conformity towards LIBs, it is an important step to understand the life-cycle of a battery [3]. Batteries age with time, where the chemistry within these cells change and thus affect the performance and capacity output. With aging, we can speak about the degradation of the cell, which is the many ways in which the cell components deteriorate in comparison to their pristine state. Degradation such as Solid electrolyte interface (SEI) layer growth, particle fractures, lithium plating, electrode decomposition and structural change impact the cell through various paths bringing about a change in the internal chemistry hindering its optimal operation. Most of these degradations are interlinked with each other, having chain reactions and aggravating each other to destabilize the cell faster under certain conditions, such as temperature, physical and electrical stress. This thesis aims is to understand and estimate these mechanisms and help curb their growth and maintain efficient operation of the cell for as prolonged as possible.

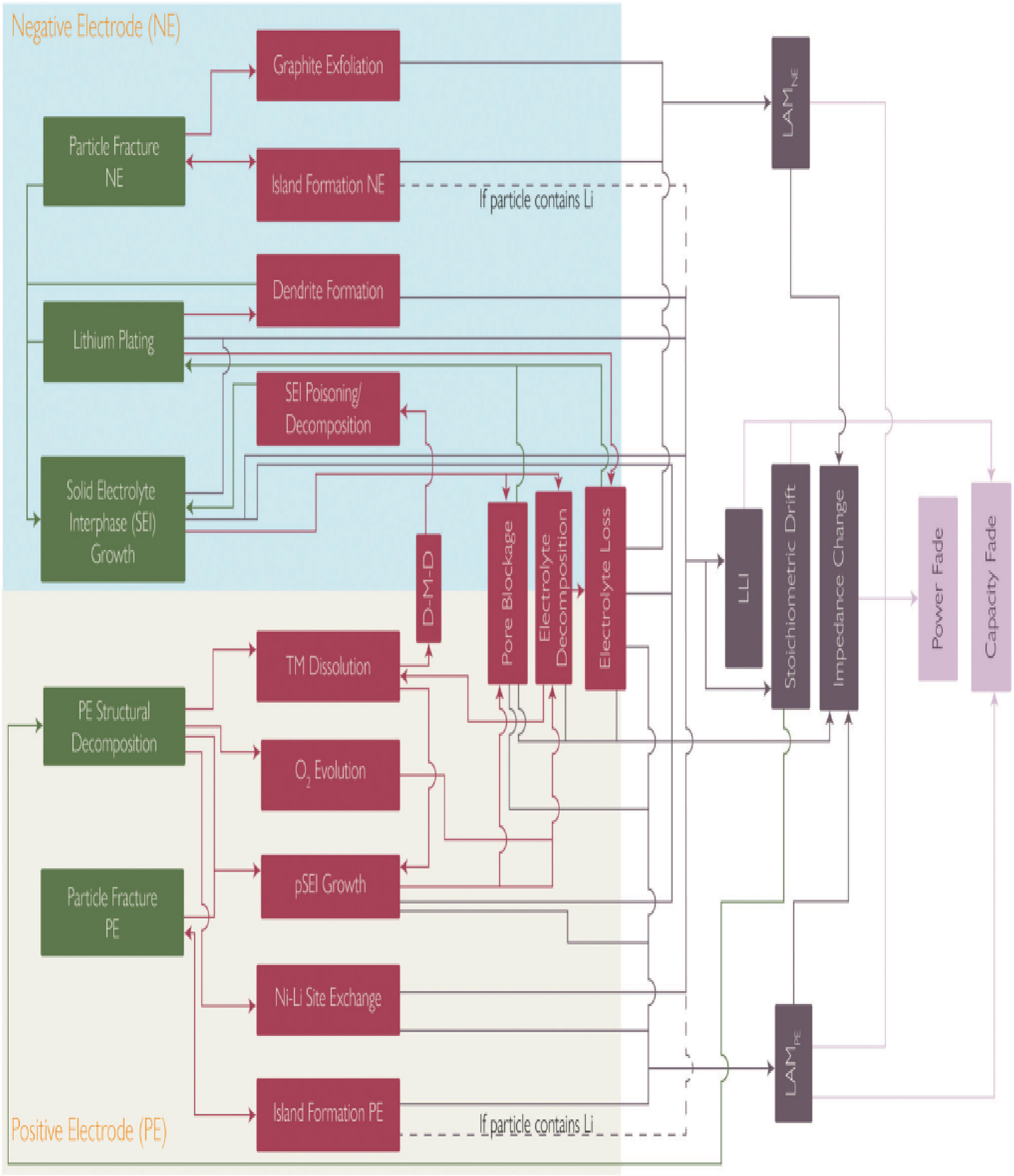

Figure 1.1: Overview of various degradation and their impacts on the Battery [3]

Fig. 1.1 gives an overview and also shows that a majority of all degradation mechanisms have impacts on the battery that can be boiled down to four major effects on the battery. Thus, a method of grouping degradation mechanisms, based on their overall impact on the cell's thermodynamic and kinetic behavior, four modes, all of which impact the thermodynamic behavior of the cell, are as follows,

- Loss of active material (LAM) (Positive and Negative electrodes). This mode groups mechanisms which lead to a reduction in the material available for electrochemical activity.

- Loss of lithium inventory (LLI), This mode groups mechanisms resulting in a reduction of cyclable lithium available for transport between electrodes.

- Stoichiometric drift/offset. This mode groups mechanisms where electrodes become imbalanced relative to each other.

- Impedance change. This mode groups those mechanisms affecting the kinetic behavior of the cell.

As important as all these modes are, the focus of this work are upon two modes for estimations of which are widely accepted over various literature, i.e.,

- Loss of active material in the positive electrode (LAM_{PE})

- Loss of active material in the negative electrode (LAM_{NE})

- Loss of lithium inventory (LLI)

These modes were chosen as they can be mathematically analyzed using battery voltage and its patterns. These modes can help understand the utilization patterns and degradation of the battery to a whole lot of accuracy.

In the context of physical experimentation, laboratories traditionally resort to the dissection of battery cells to uncover insights into their degradation processes, albeit rendering the cells non-operational after this post-analysis. However, for real-time diagnostics, reliance solely on discrete voltage, current and temperature readings obtained during operation becomes imperative [4]. Introducing a method to extract meaningful information from such limited data, the concept of Open-Circuit Voltage (OCV) plotting across State of Charge (SOC[%]) emerges as a valuable tool.

Defined as the resting, unloaded terminal voltage of a battery, OCV serves as a thermodynamic fingerprint of the electrodes at any given moment. It represents the disparity between the cathode and anode half-cell voltages and exhibits a monotonically increasing trend with battery SOC. Moreover, OCV encapsulates the unique characteristics of various degradation modes experienced by lithium-ion batteries (LIBs) and their constituent electrodes. Alterations in this fingerprint, therefore, present an opportunity to expand on the insights into the path-dependent degradation of both individual electrodes and the overarching battery cell.

The use of OCV plotting provides an effective method to understanding battery degradation dynamics, with the potential to expose important insights into the intricate processes governing LIB performance and longevity.

1.1 Purpose

In the automotive sector, the investigation and analysis of LIB degradation hold great importance for multiple compelling reasons. Initially, this pursuit is encouraged in the optimization of EV performance. Given the heavy reliance of EVs on LIBs for energy storage, a comprehensive understanding of degradation mechanisms facilitates the formulation of strategies aimed at prolonging battery life, sustaining optimal performance, and augmenting driving range. Consequently, such endeavors boost the overall competitiveness and attractiveness of electric vehicles within the automotive landscape.

Furthermore, the study of LIB degradation assumes critical significance in mitigating the financial burden on EV owners. The expense associated with battery replacement constitutes a notable concern, necessitating a thorough exploration of degradation processes. Through such investigations, automotive entities can devise innovative technologies and managerial approaches aimed at elongating battery lifespan. By diminishing the frequency of battery replacements, these initiatives effectively reduce the total cost of ownership for consumers.

Equally essential is the high standards to uphold vehicular safety standards. The degradation of LIBs presents inherent risks, including potential hazards such as thermal runaway and fire incidents. Thus, a systematic exploration of degradation mechanisms empowers automotive manufacturers to implement preemptive safety measures and deploy advanced technologies to mitigate the likelihood of battery-related accidents. Such measures are very necessary for ensuring the safety and well-being of both EV occupants and pedestrians.

Moreover, LIB degradation research assumes regulatory significance within the automotive domain. As governments worldwide enact stringent measures to curb greenhouse gas emissions and promote the widespread adoption of electric vehicles, a slight understanding of degradation phenomena becomes necessary [5]. This comprehension facilitates compliance with evolving regulatory standards pertaining to safety and environmental sustainability, thereby fostering the harmonious integration of electric mobility into existing automotive frameworks.

Lastly, the investigation of LIB degradation holds great value for the advancement of sustainable mobility solutions. Given the pivotal role of electric vehicles in mitigating carbon emissions and combating climate change, efforts aimed at prolonging LIB lifespan contribute significantly to the overarching sustainability agenda.

1.2 Objective

The project's aim can be encapsulated and outlined by the following research questions:

- Using the battery OCV data, how can the deviation from the initial OCV curve best be identified and used to describe the degradation modes?

- Can the identified deviations be used for model-based classification of modes.

1.3 Scope

This thesis aims to develop a methodology for estimating battery degradation in cars by analyzing the shift in the OCV curve. The specific aspects covered within this research include addressing the three primary degradation modes: LLI, LAM_{PE}, and LAM_{NE}. These degradation modes encompass various mechanisms such as SEI growth, SEI decomposition, electrolyte decomposition, binder decomposition, electrode particle cracking, among others. The methodology proposed in this thesis will focus on utilizing the shift in the OCV curve to estimate the progression of these degradation modes over time.

It is important to note that this research does not address the estimation of the OCV curve itself, as it is assumed that the curve data will be provided. Additionally, the causes and detailed mechanisms of battery degradation are not the primary focus here.

One of the key constraints impacting the scope is the availability of experimental data. Collecting OCV curves through laboratory experiments is a quite time-intensive and resource-intensive process. To mitigate this limitation, this thesis utilize the Python Battery Mathematical Modelling (PyBaMM) framework for generating simulated datasets. PyBaMM utilizes battery models to mathematically represent battery behavior, allowing for the generation of OCV curve data. It is acknowledged that the data obtained from PyBaMM simulations may exhibit some deviation compared to experimental data due to simplifications inherent in computational models. Furthermore, it should be noted that simulating battery cycling in PyBaMM is less computationally intensive compared to other simulation tools such as COMSOL or Matlab libraries.

2

Background on Degradation and Lithium-ion batteries

2.1 Lithium-ion Batteries

This thesis is concentrated on building the algorithm around Lithium-ion batteries. A brief general description of Lithium-ion batteries aids in understanding the working of the cell. Lithium-ion batteries serve as pivotal energy storage devices in various applications, characterized by the dynamic movement of lithium ions between the positive (cathode) and negative (anode) electrodes during charge and discharge. Comprising lithium metal oxides like lithium cobalt oxide (LCO), lithium iron phosphate (LFP), or lithium nickel manganese cobalt oxide (NMC) in the cathode and typically graphite in the anode, these batteries harness the electrochemical properties of lithium to store and release energy [6]. Facilitating ion transport between electrodes is the electrolyte, a solution housing lithium ions dissolved in an organic solvent. Ensuring electrode isolation and ion permeability is the separator, a porous membrane preventing short circuits.

During charging, lithium ions migrate from the cathode through the electrolyte to the anode, where they are stored. Conversely, during discharge, the ions reverse direction, releasing stored energy as they travel back to the cathode [7]. Lithium-ion batteries offer one of the highest energy densities among rechargeable battery technologies, making them ideal for applications where space and weight are critical factors. Lithium-ion batteries have a relatively low self-discharge rate compared to other battery chemistries, allowing them to retain their charge for longer periods when not in use. With proper care and maintenance, lithium-ion batteries can endure thousands of charge and discharge cycles, providing reliable power over an extended period.

However, despite their advantages, lithium-ion batteries pose safety concerns, notably when exposed to overcharging, overheating, or physical damage, potentially culminating in thermal runaway events. Moreover, degradation mechanisms such as electrode particle fracturing, electrolyte decomposition, and capacity fade can compromise performance and longevity over time.

In this research we focus on LG M50 cells, with simulations and parameters tailored to this specific cell. A brief description of the same is given in the following subsection.

2.1.1 LG M50 cells

Featuring a cathode composed of NMC chemistry, the LG M50 cell delivers a high specific capacity and excellent thermal stability [8][9]. This cathode formulation is optimized to balance energy density with cycle life, making it suitable for demanding applications. The graphite anode provides a stable host matrix for lithium ions during charge and discharge cycles, ensuring efficient ion transport and minimizing electrode degradation.

Table 2.1: LG M50 cell parameters

Battery Parameter [unit]	Value
Cell volume [m^3]	2.42e-05
Nominal cell capacity [Ah]	5.0
Negative current collector thickness [m]	1.2e-05
Negative electrode thickness [m]	8.52e-05
Separator thickness [m]	1.2e-05
Positive electrode thickness [m]	7.56e-05
Positive current collector thickness [m]	1.6e-05
Negative electrode porosity	0.25
Positive electrode porosity	0.335
Negative electrode conductivity [Sm^{-1}]	215.0
Positive electrode conductivity [Sm^{-1}]	0.18
Separator porosity	0.47
Initial concentration in electrolyte [$molm^{-3}$]	1000.0

With a nominal voltage typically ranging between 3.6 to 3.7 volts and a capacity spanning from 2500mAh to 3000mAh. The LG M50 cell achieves an energy density of approximately 150 to 200 watt-hours per kilogram (Wh/kg). Cycle life surpasses 1000 charge and discharge cycles under optimal conditions. Operating within a recommended temperature range of -20°C to 60°C (-4°F to 140°F), it offers versatility in various environments. The maximum continuous discharge current typically

around 10 to 15 amps and a maximum continuous charge current of approximately 5 to 8 amps.
Chen *et al.* [4] developed an extensive 35 parameter experimental data set that helped model a cylindrical 21700 LG M50 commercial cell, which is widely used in multiple applications of research. The model is also commonly called a pseudo-two-dimensional (P2D) model. Chen *et al.* parameters are used as a base parameter set in PyBaMM. It is also used as a modified parameter set by O'Kane *et al.* [2]. Some of the most important parameters considered are as mentioned in Table. 2.1.

2.2 Battery Degradation

Lithium-ion batteries have significantly impacted various fields, particularly portable electronics. Their influence extends to driving significant changes in electric vehicles and fixed energy reserves. However, the rigorous operational demands placed on batteries in these applications necessitate enhanced longevity and safety benchmarks. Consequently, there has been a notable surge in research focusing on unraveling the intricate physics underlying battery degradation. A comprehensive understanding of this phenomenon is indispensable for achieving cost-effective decarbonization aims in energy networks and transit. The ability to accurately predict lithium-ion battery degradation holds substantial economic promise, potentially yielding billions for industries worldwide, including automobile sector, aircraft industry and energy storage. Such predictive capabilities promise to elevate performance standards, bolster safety measures, and mitigate warranty liabilities effectively [3][2].

As the demand for LIBs skyrockets, driving costs down, it's equally imperative to focus on enhancing their longevity. This not only boosts their economic value over time but also lessens environmental footprints linked to material extraction and manufacturing. Understanding battery degradation is the direct connection for prolonging their operational life. Accurately predicting battery end-of-life (EoL) is pivotal for reducing or avoiding the risks of thermal runaway, ensuring safer usable operations.

Over time and with use, the impedance of LIBs increases at the same time as the total energy storage capacity diminishes [10]. This degradation arises from a variety of mechanisms, some occurring simultaneously or even triggering additional degradation pathways. Certain operation habits and operating environments can accelerate degradation via one or more processes, and the intricate interplay between these mechanisms remains incompletely understood [11].

Research efforts led by Birkl *et al.* [7] have shed light on the profound impact of stress factors on the underlying physical degradation mechanisms. Furthermore, comprehensive models, as examined by Reniers *et al.* [11], have provided insight into the intricate interplay of these degradation processes. Among the stress factors, temperature stands out as paramount, with deviations from the standard 25°C potentially accelerating the degradation process. Operating the battery at higher State of Charge (SoC) levels(above 70%) increases degradation due to the correlation between electrode potentials and the occurrence of parasitic side reactions.

Moreover, high current operation amplifies the risk of failure by inducing mechanical stresses within the battery during cycling. Additionally, it promotes lithium plating during charging, further contributing to degradation. This dual effect underscores the importance of carefully managing operating conditions to mitigate degradation and prolong battery lifespan. Understanding the nuances of these stress factors and their implications for degradation is crucial for optimizing battery performance and ensuring long-term reliability across various applications.

The extent of these influences is also contingent upon secondary factors, including subtle manufacturing imperfections. For instance, Harris *et al.* [12] demonstrated the variability in the lifespan of 24 apparently identical pouch cells, all subjected to the same cycling regimen. While the exact cause of this variability remains unknown, it is probable that minor deviations in manufacturing conditions contributed to it, underscoring the importance of manufacturing procedures and accuracy. Also noting, factors such as the application of external pressure to pouch cells or the development of thermal gradients due to internal heat generation can significantly impact performance and degradation.

Recent studies [13][14] have increasingly emphasized the critical role of path dependence [15], revealing how various degradation mechanisms come into play. These mechanisms may become active during calendar aging, characterized by the battery being at rest, or during cycle aging, occurring during active usage or charging. Real-world usage patterns often involve a blend of rapid (dis)charging, slower (dis)charging, or periods of idleness. Consequently, exploring this phenomenon in depth becomes imperative for enhancing the accuracy of battery lifespan predictions.

In the world of LIBs, there's a notable absence of a fully comprehensive model that encompasses all effects and their interplay. While researchers have attempted to connect these mechanisms, like the impact of SEI layer growth on pore blockage and lithium plating rate, leading to a nonlinear drop in capacity, a complete understanding is still lacking. Moreover, the importance of path-dependency—specifically, which mechanism triggers first—is often underestimated. This sequence significantly affects lifespan, particularly under higher current loads. Accurately capturing these complex relationships proves challenging with empirical models, highlighting the need for physics-based approaches.

At the most intricate level are degradation mechanisms, which elucidate the physical and chemical changes occurring within the cell, including electrode degradation, electrolyte decomposition, and the formation of SEI. Observing these mechanisms directly during battery operation poses challenges due to the complexity of battery processes and limitations in observation techniques. Nonetheless, researchers employ advanced tools like microscopy and spectroscopy to gain insights [16].

Transitioning to a more observable perspective, capacity fade and power fade represent tangible outcomes of degradation. Capacity fade entails a gradual reduction in the cell's usable capacity over time, limiting its energy storage and delivery capabilities. Power fade, on the other hand, involves a decrease in the battery's deliverable power following degradation, impacting its ability to meet power demands. While offering a less detailed view compared to degradation mechanisms, capacity fade and power fade serve as practical metrics for evaluating battery health and performance, facilitating optimization efforts by manufacturers and researchers.

The following section presents a concise and coherent breakdown of the primary mechanisms affecting lithium intercalation materials. It establishes connections between degradation mechanisms and their activation conditions while highlighting the intricate relationships among them. Recognizing these interactions is pivotal, as the combined effects of mechanisms may not always be replicated by considering them individually. Although empirical models may attempt to capture this complex interplay, their effectiveness in preventing degradation is limited without integration with physics-based models.

While a multitude of degradation mechanisms exist, it is not necessary to encompass every known process. Instead, emphasis should be placed on mechanisms generally regarded as most impactful during regular battery operation. Other recognized degradation processes, as shown in Fig. 2.1 include phenomena such as salt precipitation, binder decomposition, and electrode-current collector delamination, among others.

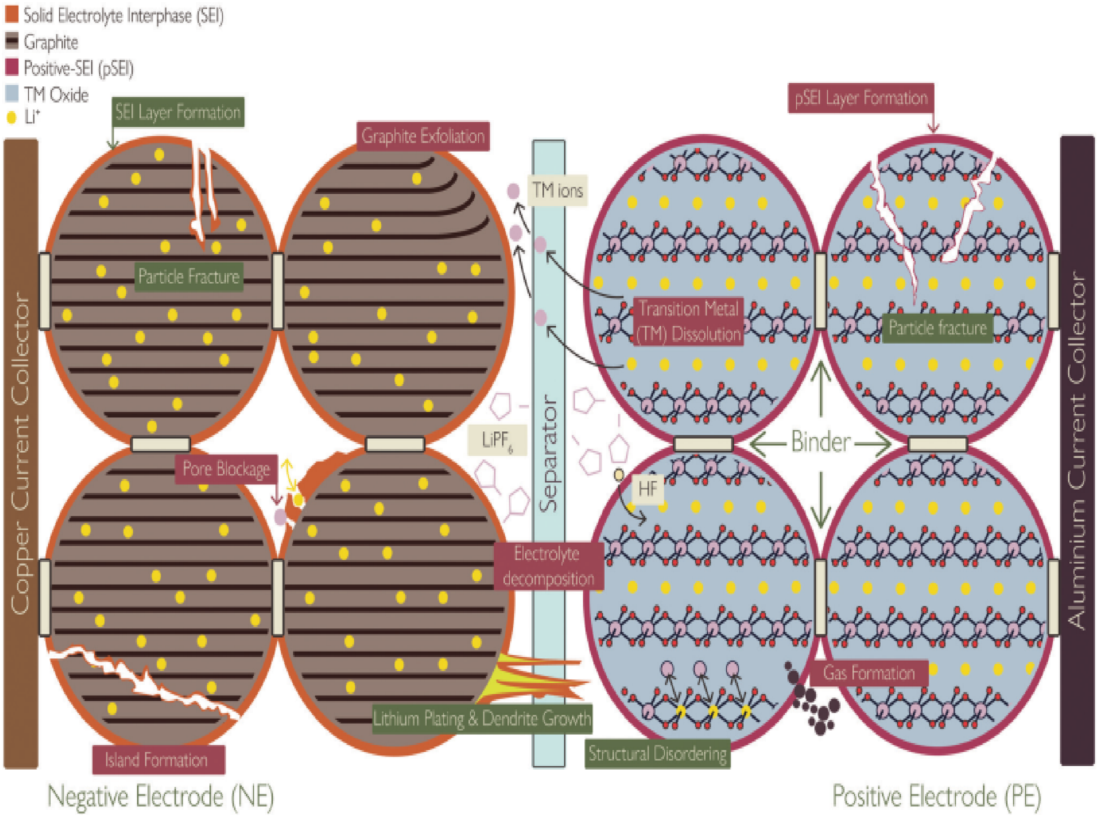

Figure 2.1: Various degradation processes in the Battery [3]

2.2.1 SEI Layer growth

SEI layer stands as a pivotal component governing the efficacy and endurance of lithium-ion batteries. Acting as a protective shield on most negative electrode surfaces, the SEI emerges upon the initial interaction of the liquid electrolyte with the conductive surface of the negative electrode. This layer, possessing characteristics very much similar to a solid electrolyte, serves to reduce further electrolyte degradation and curb undesirable side reactions. However, the formation of the SEI comes at a cost: irreversible capacity loss occurs as cyclable lithium becomes ensnared within its structure.

An important concern is the unexpected fear of the SEI to grow, the phenomenon is accelerated by elevated temperatures and high current regimes. Even during periods of cell rest at high SOC, although at slower rates, the SEI continues its expansion, consuming electrolyte solvents and diminishing both electrolyte quantity and conductivity. Furthermore, the decomposition of the SEI at elevated temperatures can escalate to catastrophic thermal runaway events.

Experimental methodologies devised that can help detect and monitor SEI layer growth [3]:

- High Precision Coulometry (HPC)

- Electrochemical Impedance Spectroscopy (EIS)
- Hybrid Pulse Power Characterization (HPPC) tests

The effects of SEI growth range mainly around:

- Loss of lithium inventory
- Increased impedance.

Fick's law [2] emerges as a cornerstone in the modeling of SEI layer growth, providing a framework for understanding its complex dynamics.

2.2.2 Lithium Plating

Lithium plating, a side reaction observed in lithium-ion batteries, involves the formation of metallic lithium on the negative electrode surface rather than its intercalation into the electrode material. This phenomenon is particularly prevalent at low temperatures, where the main intercalation reactions slow down, even at moderate charging or discharging rates. Factors such as high SOC, high current or charging rates, elevated cell voltages, and insufficient negative electrode mass or electrochemically active surface area can all contribute to lithium plating. Detecting and quantifying lithium plating often involves various experimental approaches [3]:

- Resistance-capacity plots
- Arrhenius plots to extrapolate behavior across temperature ranges
- Monitoring high capacity fade over cycles.

Fast charging at low temperatures is a primary trigger for lithium plating, with higher charging currents and voltages exacerbating the phenomenon. Despite its adverse effects on battery performance, lithium plating can be reversed through the inverse reaction known as stripping. Understanding and mitigating lithium plating are critical for optimizing battery operation and longevity, particularly in applications where low temperatures and rapid charging are common.

2.2.3 Electrode decomposition

Several complex degradation mechanisms impact lithium-ion battery positive electrodes. These include phase transitions in delithiated NMC oxides, which release oxygen reacting with the electrolyte. Additionally, oxidation of lattice oxygen within the cathode material contributes to degradation. High oxidation states destabilize nickel, causing it to dissolve into the electrolyte. Crystal lattice alterations between lithium and nickel affect electrode integrity, while transition metal ions form deposits on the positive electrode surface, compounding degradation.

Experimental evidence suggests that elevated temperatures and high voltages promote transition metal dissolution and eventual precipitated solid electrolyte interface (pSEI) formation. Techniques for confirmation include [3]:

- Visualization of reconstructed disorder layers during phase transformations using atomic resolution ADF-STEM imaging.

- Online electrochemical Mass Spectrometry (OEMS) reveals heightened delithiation and oxygen release at room temperature.

- Tracking phase changes in NMC materials through peak analysis in cyclic voltammetry at higher voltages (3.0 - 4.8V) and standard electrochemical characterization.

Understanding and mitigating these degradation mechanisms are crucial for optimizing lithium-ion battery performance, longevity, and safety, particularly in applications subjected to high temperature and voltage conditions.

2.2.4 Particle fracturing

Particle fracturing is a prevalent phenomenon in both positive and negative electrodes of lithium-ion batteries, driven by significant volume changes of electrode materials during electrochemical operation, leading to stress accumulation. Localized particle fragmentation, particularly near the separator, is attributed to higher local current densities causing elevated stresses. Notably, silicon electrodes exhibit pronounced particle cracking, even with minimal silicon content, resulting in markedly low cycle lifetimes [3].

The ramifications of particle cracking are multifaceted:

- Disruption of electrical contact between active particles, conductive additives, and current collectors leads to diminished electronic and ionic conductivity, ultimately contributing to capacity fade.

- Particles beyond a critical size threshold experience fracture, disintegrating into isolated islands.

- Elevated stress levels correlate with accelerated formation rates of SEI and precipitated solid electrolyte interphase (pSEI), directly impacting the rate of capacity loss.

- Electrolyte pulverization occurs as small cracks in the electrode propagate, separating some active material from the particle ensemble, resulting in capacity fade.

Operating under extreme temperatures, both above room temperature and sub-zero conditions, accelerates electrode particle fracture. Certain cycling conditions, such as graphite staging, can further exacerbate fracture rates.

Experimental methods for studying particle fracturing include [3] :

- X-ray computed tomography (XCT)
- Stress/strain measurements at the stack level to assess failure
- Differential Voltage Analysis (DVA) for determining LAM in the electrodes.

Understanding and mitigating particle fracturing are paramount for enhancing lithium-ion battery performance and longevity, particularly in demanding operating conditions.

3

Background on Degradation Mode Analysis

With the introduction of lithium-ion batteries into the industry, its complexities and downfalls have to be considered at length to aid its most efficient usage. Through the previous chapter, an overview towards lithium-ion batteries, how they work and how they degrade were explained. This brings light towards the end effects of the various degradation processes - degradation modes. The three main degradation modes this project has considered are LLI, LAM_{PE}, LAM_{NE}.

In the world of lithium-ion batteries, F Brosa Planella *et al.* [1] revealed the complex world of physics-based electrochemical battery models. Starting from the basics of porous electrode theory, these models become powerful tools. They don't just uncover the hidden parameters/states in lithium-ion batteries; they also help shape in designing them and improve their performance. The authors stress the importance of adjusting the model's complexity to fit different uses, highlighting how designing batteries requires a lot more computational power compared to the on-the-fly control needed in electric vehicles.

Their contribution revolves around an intriguing reductive framework that is revealed in the review. Beginning with a high-fidelity microscale model, the authors methodically navigate through layers of complexity, moving down to the simplicity of the single particle model. This reductionist approach unveils an interconnected web, linking seemingly disparate models in the literature, including the well-known Doyle–Fuller–Newman model (DFN). The paper presents various models and provides a critical assessment of their advantages and disadvantages, acting as a guide for choosing the right model for a given set of circumstances.

O'Kane *et al.* [2] focused on the development of experimental techniques for parameterization of multi-scale lithium-ion battery models. They discuss the challenges of overfitting when fitting aging data and the importance of degradation mode analysis for validating lifetime prediction models. The authors emphasize the need to go beyond validating models against capacity and power fade, highlighting the significance of degradation mode analysis involving various degradation mechanisms in lithium-ion batteries.

Jacqueline S. Edge *et al.* [3] provide a comprehensive examination of the factors contributing to the degradation of lithium-ion batteries, crucial components in modern technology ranging from portable electronics to electric vehicles. The paper focuses on describing the fundamental principles of lithium-ion batteries and their widespread applications, before delving into the mechanisms underlying battery degradation, including chemical reactions, mechanical stresses, and thermal effects. It delves into the intricacies of degradation processes occurring within the battery, such as electrode/electrolyte interactions, structural changes in electrode materials, and the formation of undesirable compounds during charge and discharge cycles. Edge *et al.*. highlights the diverse array of factors influencing degradation, such as operating conditions and battery design, and discusses diagnostic techniques for monitoring battery health. Additionally, the paper explores mitigation strategies, such as material improvements and advanced battery management systems, aimed at prolonging battery lifespan and enhancing performance. Sion E. J. O'Kane *et al.* [2] delve further into elucidating degradation mechanisms, including the conditions that trigger them and their repercussions on battery performance. Their comprehensive descriptions encompass collaborative degradation processes that mutually influence one another, as well as individual degradation mechanisms aimed at destabilizing the battery or leading to capacity or power loss. These explanations are accompanied by mathematical models that account for a variety of external and internal factors. O'Kane *et al.* meticulously craft these equations not only to address the isolated causes and consequences of degradation but also to capture the interplay between different degradation mechanisms. The paper culminates in the application of these equations through simulations conducted on PyBaMM, offering a synthesized understanding of battery degradation dynamics.

The various degradations being classified into the three modes as mentioned in the above section, leads to the use of OCV curves to analyze the aging and degradation of the battery. Chang-Hui Chen *et al.* [4] mentions that Galvanostatic Intermittent Titration Technique (GITT) is a method used in electrochemical studies to understand both how fast reactions occur (kinetics) and the overall energy landscape (thermodynamics) of the system being investigated. GITT involves applying a brief burst of current to change the charge state of the cell, followed by a long rest period where the cell sits without any current flowing through it. This resting period lasts either for a predetermined time or until the system reaches a stable equilibrium, indicated by a nearly constant voltage. This process is repeated across different voltage levels of interest. By recording the voltages at the end of each rest period, researchers can determine the Open Circuit Voltage (OCV) of the cell, known as the GITT-OCV. Additionally, analyzing the current-voltage profiles obtained during GITT allows for the calculation of diffusion coefficients, providing insights into how ions move within the cell at various states of charge.

With an emphasis on the complex behavior resulting from LAM [17] in both positive and negative electrodes, this work explores the detailed modeling and simulation of lithium-ion batteries. The used model is very detailed, taking into account intricate electrode designs and feeding characteristics from half-cell data into an ECM. The simulation explores sub-ECMs that represent active material compositions in various configurations and takes into account a variety of electrode compositions. The integrity of the model in simulating discharge curves and polarization resistances for a range of charging rates is demonstrated by validating its correctness against experimental data. The study's consideration of LAM degradation scenarios, such as lithiated and delithiated states in both electrodes, is an important component. The impact of deterioration on loading ratios, electrode-specific rates, and the charge states at the conclusion of the discharge and charge cycles are also examined in this paper.

J. Schmitt *et al.* [18] and C. R. Birkl *et al.* [7] propose two various ways to implore the OCV curve and extract degradation mode parameters. J. Schmitt *et al.* present a novel approach employing a model that facilitates the identification of degradation modes based on the half-cell voltage during low-current charging and discharging. This method involves aligning the Open-Circuit Potential (OCP) curves of both electrodes with the full cell OCV curve until the discrepancy between the pristine OCP curves matches the measured full cell OCV curve. The adjustment parameters, i.e., linear scaling (α) and shifting (β) of the electrode OCPs, are directly linked to the specific degradation modes LLI, LAM_{PE}, and LAM_{NE}. C. R. Birkl *et al.* [7] endeavor to model the OCV and OCP curves of lithium-ion cells using the Nernst equation in their pristine state, in order to extract key parameter values. Applying the same model equation to the measured OCV of degraded cells, employing to obtain the fit parameters. By examining the differences in these parameters, one can establish non-linear correlations with specific degradation modes. Birkl *et al.* [7] validate this approach by considering various degradation mechanisms across different stages of cell aging, ultimately providing estimations of degradation modes that closely align with experimental observations.

Karger and Schmitt *et al.* [19] mechanistic calendar aging model is an innovation in prognosticating battery health. Departing from conventional capacity-centric approaches, this model delves deep into the component states of health, explaining the complex degradation mechanisms. Through thorough experimentation spanning over 672 days under diverse storage conditions, the authors presented the pivotal roles of ambient temperature and SOC in battery aging. Their two-step compensation strategy addresses degradation effects from periodic check-ups, while the utilization of Tafel and Arrhenius equations shows the temperature and SOC dependencies of degradation with atmost clarity. This model not only enhances the predictability but also underscores the importance of temperature and SOC in understanding battery aging dynamics, laying a robust foundation for future research and practical applications.

Meanwhile, C. Zhu and L. Sun *et al.* [20] study introduces a new approach to degradation diagnostics and State of Health (SoH). estimation by harnessing the latent potential of half-cell electrode potentials. By scrutinizing the voltage differentials between individual electrodes and a reference electrode, this approach overcomes the limitations of conventional methods, offering a microscopic view into degradation phenomena such as lithium plating and SEI layer evolution. Through rigorous validation against extensive experimental data, the authors demonstrate the method's efficacy in discerning between various degradation mechanisms, elevating SoH estimation accuracy to high levels. In parallel, Kirkaldy and Samieian *et al.* [21] exhaustive investigation into LIB degradation dynamics, spanning 40 LG M50T 21700 cells under 15 diverse operating conditions, unveils invaluable insights into commercial cell behaviors. Their meticulous experimental design, culminating in around 33,000 equivalent full cycles, provides a rich data illuminating the multifaceted facets of degradation in these cells, offering guidance for future research and industrial applications. Pietro Iurilli and Claudio Brivio *et al.* [22] meticulous methodology for SoH estimation, leveraging EIS and the distribution of relaxation times (DRT), epitomizes precision and accuracy. With a mean absolute error of less than 0.75% for SoH values above 85%, and less than 3.70% for SoH values between 85% and 80%, their approach in battery health management, offering a robust framework for real-world applications.

In the quest for real-time battery monitoring, Zhou and Zhang *et al.* [23] on-the-fly computing approach for OCV estimation revolutionizes traditional methods by drastically reducing measurement time without compromising accuracy. By circumventing the need for complete voltage relaxation information, this method helps in the improvement of efficiency and precision in battery diagnostics, offering tangible benefits for dynamic battery management systems.

Moreover, Dubarry and Truchot *et al.* [24] comprehensive mechanistic model, integrating multiple degradation scenarios and leveraging Incremental Capacity Analysis (ICA) for degradation feature identification, embodies a holistic approach to battery health management. By diagnosing existing degradation and prognosticating future performance under diverse operating conditions, this model offers a roadmap for predictive maintenance strategies, ensuring the longevity and reliability of battery systems.

Lastly, Yang and Zhang *et al.* [25] innovative methodology, leveraging partial charging data for voltage curve reconstruction and SoH estimation, represents a paradigm shift in efficiency and accuracy. By harnessing statistical and machine learning techniques, their approach streamlines the SoH estimation process, offering a scalable solution adaptable to diverse battery systems.

This project aims to simulate battery aging and degradation which can help in analyzing and computing real life data for calculating the extent of the degradation modes. For this purpose, a Python library, PyBaMM [26] is being used. It is an open-source Python package tailored for modeling and simulating LIBs. It allows for flexible model construction, incorporating fundamental physics principles to accurately capture battery behavior. It can be used for various applications by changing parameters of batteries being used and experimental simulations.

Collectively, these studies of precision and insight in LIB degradation research, offering a variety of methodologies and insights that help to reshape the ongoing research of battery technology.

4

PyBaMM

4.1 Introduction:

PyBaMM [26] is an open-source battery simulation package written in Python. It serves as a fast and flexible tool developed to accelerate research in the battery field by multiple researchers from various universities such as the University of Oxford, the University of Michigan, Imperial College London, etc. It is a modular platform for researchers to model various aspects of batteries, such as electrochemical processes, thermal management, and degradation mechanisms.

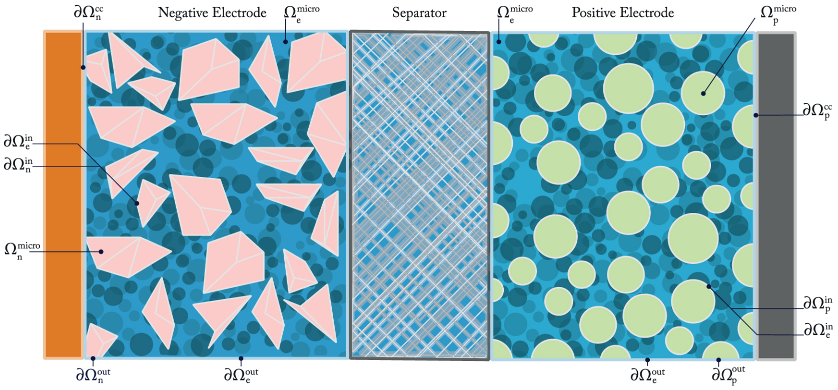

Figure 4.1: Micro Scale Model [1].

PyBaMM consists of different models representing the battery from high-fidelity microscale models (see Fig. 4.1) [1], reduced to a macro model (see Fig. 4.2). At the microscale level, the components inside the cell are modeled very close to reality, but this leads to high computational costs, whereas the macro model represents the cell in a more simplified format, which is computationally less expensive and can be implemented in real-time models.

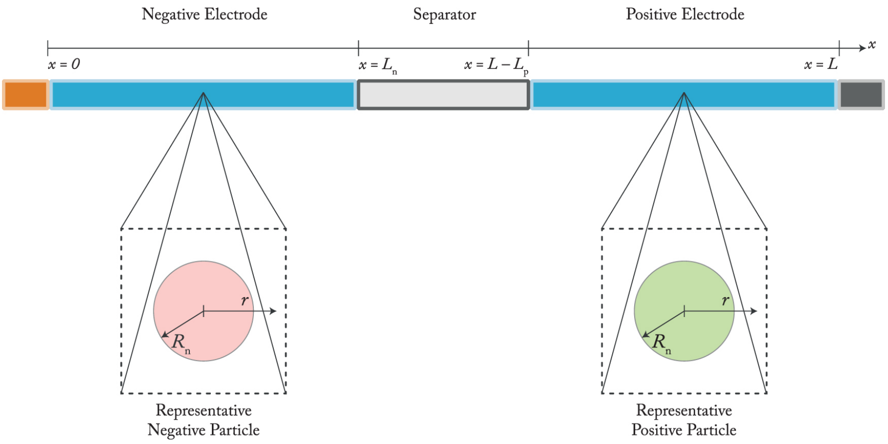

Figure 4.2: Macro Scale Model

Comparisons can be easily performed to understand the behavior of the cell based on the model or by changing the cell parameters. High charge and discharge experiments can be performed on cells by varying voltage and current to understand cell capacity retention and how cells degrade over numerous charge and discharge cycles, providing insights into their expected lifespan. Different thermal models are available to study the thermal behavior of the cell, such as isothermal and lumped thermal models [27][28], both of which can be used with any cell geometry, as well as a 1D thermal model [27][28] which accounts for through-cell variation in temperature in a pouch cell.

All models in PyBaMM have default solvers, typically differing depending on whether the model results in a system of ordinary differential equations (ODEs) or differential algebraic equations (DAEs). One of the most common options you may want to change is the solver tolerances. By default, all tolerances are set to 10^{-6}. However, depending on your simulation, you may find you want to tighten the tolerances to obtain a more accurate solution, or you may want to loosen the tolerances to reduce the solve time. Additionally, it allows users to create their own models and algorithms, contributing to the development of the PyBaMM git repository.

Similarly, additional physics can be incorporated into existing models through an extensible plug-and-play sub-model structure around which the models are constructed. As a result, the need to create desired models from scratch is eliminated, as specific sub-modules can be pulled, and new physics and constraints can be added. For example, coupling together several degradation mechanisms is readily achieved.

In this thesis, PyBaMM is used as a tool for generating datasets for various degradation stages of battery cells through simulation under diverse cycling conditions. The reason behind choosing PyBaMM as the tool to generate the dataset is to substantially reduce the time and cost associated with real-time chamber testing. By simulating battery behavior for various cycles and under differing environmental and operational parameters, PyBaMM offers a cost-effective and efficient means of comprehensively exploring the intricacies of battery degradation and behaviour as the battery is aging. Leveraging PyBaMM for data generation not only accelerates research progress but also facilitates deeper insights into the underlying mechanisms governing battery performance and aging.

4.1.1 Parameters Sets

Parameter set is a collection of values that defines the physical properties and characteristics of the cell.These parameters include properties such as electrode physical dimensions, material diffusion coefficients, decay rate, initial material concentration in each electrode, etc. Parameter sets are essential for constructing battery models because they define the behavior of the system being simulated. These parameters set are created using experimental data from GITT, Cyclic Voltammetry (CV), etc. PyBaMM provides various pre-defined parameter sets for different types of batteries, such as lithium-ion batteries, lead-acid batteries, etc.

Table 4.1: A summary of physics-based model parameterisations of commercial cells in literature.

Paper	Cell Type	Wh/kg	Chemistry
Chen 2020[4]	5 Ah LG cylindrical 21700	267	NMC811 graphite-SiOy
O'Regan 2022[29]	5 Ah LG cylindrical 21700	267	NMC811 graphite-SiOy
Ecker 2015[30][31]	7.5 Ah Kokam pouch	173	NMC111 graphite
Mohtat2020[32]	pouch cell		NMC532 graphite
Prada2013[33]			$LiFePO_4$ graphite
OKane2022[2]	5 Ah LG cylindrical 21700	267	NMC811 graphite-SiOy

Some of the parameter sets available in PyBaMM are listed in Table 4.1. The parameter set is created using the research papers mentioned in Table 4.1 In this research work they worked on identifying the cell parameter by experimental method. The parameter identified using the experimental method is used to model the cell.

In the present study, the decision was made to use the NMC811 cell chemistry, as its specifications align with those of the cells utilized in Volvo cars. However, as depicted in Table 4.1, four parameter sets have been derived for this cell chemistry. After careful consideration, the OKane2022 [2] parameter set was selected. This decision was informed by its development methodology, which takes into account the intricate interplay among various degradation pathways within a single electrode. The OKane2022 parameter set leverages the DFN [1] model, a topic that will be expanded upon in the subsequent subsection. Notably, the DFN model employed in OKane2022 is founded upon the work of Chen *et al.* (2020), who meticulously assembled a comprehensive dataset comprising 35 parameters from experimental observations of a cylindrical 21700 commercial cell. These parameters encompass a wide array of chemical, physical, electrochemical kinetics, and thermodynamic properties of the cell.

The Open Circuit Potential (OCP) data for the individual electrodes used in the OKane2022 parameter set is derived from the work of Chen *et al.* (2020). This dataset offers insights into the lithium content within each respective electrode. Chen *et al.* (2020) conducted experiments to examine the behavior of individual electrodes during (de)lithiation, represented by plotting OCP curves as a function of stoichiometry, defined,

$$x_{PE/NE} = \frac{C_s}{C_s^{max}} \tag{4.1}$$

where $x_{PE/NE}$ is the stoichiometry for cathod(Positive)/anode(Negative) electrode, C_s is the lithium concentration and C_s^{max} is the maximum lithium concentration in the electrode.

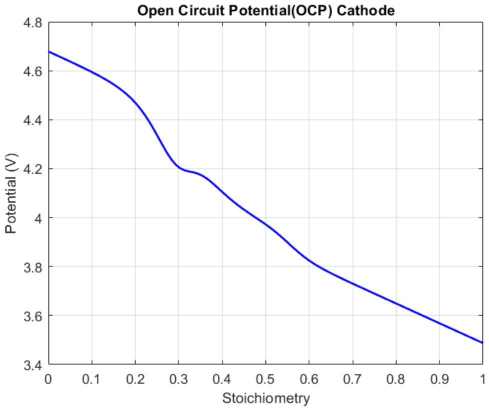

Figure 4.3: OCP Cathode

Figure 4.3 illustrates the voltage($U_{PE}(x_{PE})$) behavior of the individual cathode electrode, also referred to as the positive half-cell, as it transitions from a delithiated state (with x_{PE} value of 0) to a lithiated state (with x_{PE} value of 1). A x_{PE} value of 0 signifies the absence of lithium in the positive electrode, indicating a fully charged battery, whereas a x_{PE} value of 1 indicates a fully discharged battery.

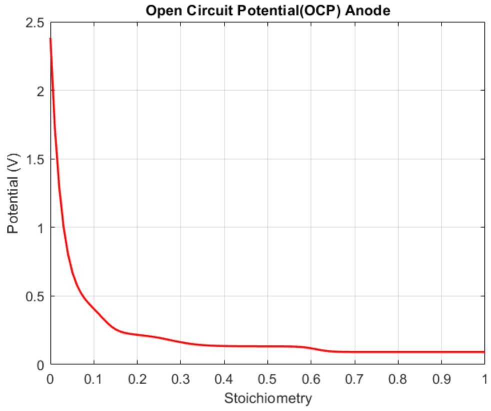

Figure 4.4: OCP Anode

Similarly, the data for the negative half-cell is depicted in Figure 4.4. Here, a x_{NE} value of 0 indicates the absence of lithium in the negative electrode, representing a fully discharged battery, whereas a x_{NE} value of 1 signifies a fully charged battery. Chen *et al.* (2020) formulated an expression, depicted above, capable of fitting the experimental curves for both the anode (NE) and cathode (PE):

$$\begin{aligned} U_{PE}(x_{PE}) = & -0.8090 \cdot x_{PE} + 4.4875 \dots \\ & -0.0428 \cdot \tanh(18.5138(x_{PE} - 0.5542)) \dots \\ & -17.7326 \cdot \tanh(15.7890(x_{PE} - 0.3117)) \dots \\ & +17.5842 \cdot \tanh(15.9308(x_{PE} - 0.3129)) \end{aligned} \tag{4.2}$$

$$\begin{aligned} U_{NE}(x_{NE}) = & 1.9793 \cdot e^{-39.3631 x_{NE}} + 0.2482 \dots \\ & -0.0909 \cdot \tanh(29.8538(x_{NE} - 0.1234)) \dots \\ & -0.04478 \cdot \tanh(14.9159(x_{NE} - 0.2769)) \dots \\ & -0.0205 \cdot \tanh(30.4444(x_{NE} - 0.6103)) \end{aligned} \tag{4.3}$$

4.1.2 Model

A set of mathematical equations which mimic the real life battery behaviour is called a model. How detailed the battery is modelled defines its complexity, accuracy of output and computation cost for simulation. Currently, PyBaMM offers various complex models that tries to capture real cell behavior. The models below were considered in this study.

- Doyle-Fuller Newman (DFN)

- Single Particle Model with Electrolyte (SPMe)
- Single Particle Model without Electrolyte (SPM)

The DFN model, also known as the pseudo-two-dimensional (P2D) or Newman model [1], is the most popular physics-based model for lithium-ion batteries. The primary distinction between the microscale model and the DFN lies in their treatment of electrode particles. In the DFN model, we assume that all electrode particles are equal and have a spherical structure. For instance, in Fig. 4.1, it is illustrated that electrodes are modeled as three-dimensional porous structures with varying shapes along the length of the electrode. In contrast, the DFN model, as shown in Fig. 4.5, assumes a one-dimensional spherical particle structure within the electrode, maintaining a constant radius along the electrode length. This simplification reduces the model to a one-dimensional planar geometry. Additionally, the electrodes and separator are presumed to possess a one-dimensional planar geometry. This simplification renders the model computationally feasible while retaining enough of the physics to accurately predict battery behavior and capture its internal states.

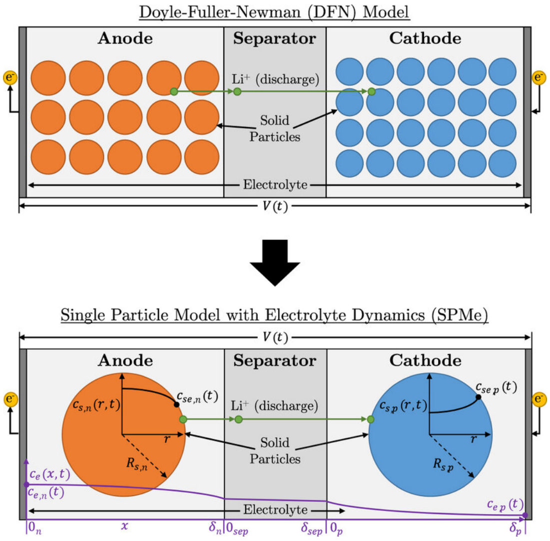

Figure 4.5: Schematic of DFN and-SPMe model [1]

SPM's [1] models are simplified versions of DFN models. In SPM's, the electrodes are represented as single spherical particles, assuming uniform lithium concentration and potential for all particles. The SPM's can be categorized into two types: one that takes into account electrolyte dynamics, known as the SPMe model, and another that does not take electrolyte dynamics into account, known simply as the SPM model. The key difference between SPMe and SPM is that potential drops across the electrolyte are considered in SPMe, whereas they are neglected in SPM.

In this work it was decided to go with the DFN model over the other models due to higher accuracy, particularly for predicting battery degradation, performance and thermal behavior. This choice is crucial as the data generated will serve as input for a degradation mode estimation algorithm, with the degradation mode data from PyBaMM used as ground truth for benchmarking the algorithm's estimation. Further discussion on this matter will be provided in subsequent chapters. It is noteworthy that the OKane2022 parameter set is developed based on the DFN model.

4.2 Simulation

This section details the conditions considered in the simulations aging the cell. We start off with no thermal model included, i.e., the temperature is assumed to be constant.

4.2.1 Standard Cycling Protocol

To age the pristine cell, a cycling procedure [2] is conducted in a chamber testing environment. In this procedure, the cell is charged and discharged at certain constant voltages or currents while varying the ambient temperature in the chamber, which may trigger degradation mechanisms. To replicate the experimental behavior through simulation, a similar cycling protocol is followed. Additionally, specific options in the model must be specified or activated to indicate degradation mechanisms, which will be discussed in the next subsection.

In the simulation environment before cycling, the cell is always initialized to a pristine condition and fully charged. The pristine, fully charged cell undergoes the following steps: First, it is cycled as per the requirement, then it is held at the same voltage for a certain number of hours without any load. Subsequently, a constant small load is applied, and the battery is allowed to relax for a certain number of hours. After relaxation, voltage readings are collected. The reason for allowing the battery to relax before collecting readings is to mitigate the polarization effect, such as ohmic and activation polarization recovery. Ohmic polarization results in a voltage drop across internal resistance, which reduces rapidly, restoring the cell to its OCV. Activation polarization, due to kinetic limitations, recovers more slowly as electrochemical reactions resume.

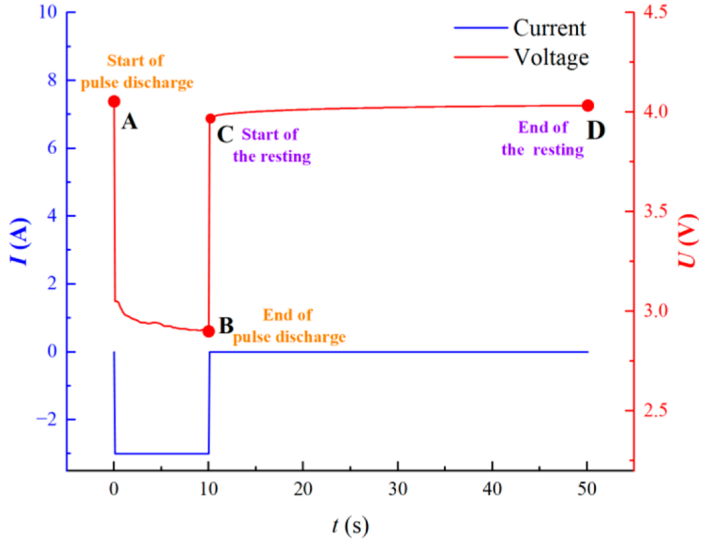

Figure 4.6: Polarization effect [34]

As shown in Fig. 4.6, taking voltage readings immediately after the end of a pulse discharge may result in deviations. To overcome this, the battery is rested for a longer duration, and voltage readings are collected at the end of the resting period when the voltage reading would have settled. The cycle of pulsating discharge, relaxation, and voltage data collection is repeated multiple times until the battery reaches its cutoff voltage, typically set at 2.6V. This process results in the generation of an OCV curve.

Listing 4.1: Experiment setup for battery cycling.

```
totalcycles = 1000 % Number of cycles.
totalpulse = 200 % Number of pulsating discharge.

%%%% Standard cycling protocol %%%%
experiment = pybamm.Experiment(
    [(
        "Discharge at 0.5A until 2.6 V",
        "Charge at 1.5A until 4.2 V",
        "Hold at 4.21 V until 50mA",
    )]* totalcycles  % First step cycling the cell.
    +

    ["Rest for 4 hours"] % Resting Period.
    +

    [
        "Discharge at 0.125A for 0.5 hours",
        "Rest for 3 hours"
```

```
    ]* totalpulse, % Pulsating discharge collecting OCV data.

    termination= "2.6 V" % Experiment termination volatge.
)
```

The cycling protocol, as previously explained, is depicted in the Listing 4.1, demonstrating how it is implemented in PyBaMM. Firstly, the cell is cycled according to the procedure outlined in Listing 4.1. This procedure is repeated as specified by the variable ’totalcycles’. Following the cycling, the cell is rested for the resting period as stated. Subsequently, pulsating discharge is applied to collect OCV curve data, and this process is repeated as indicated by the variable ’totalpulse’ until the termination voltage is reached.

4.2.2 Degradation Mechanism

To age/degrade a battery and collect data of loss of active material in positive and negative electrode, and loss of lithium inventory, in PyBaMM the cell has to be cycled as per the standard cycling protocol degradation mechanism modes turned on according to model options. There are many degradation mechanism available but not all the options are compatible with each other and with all the models implemented in PyBaMM. This report would only discuss about degradation modes which are found suitable for this specific model and parameter set after extensive simulation trail and study.

"SEI:solvent diffusion limited"[35] is a degradation mechanism in PyBaMM which will initiate the SEI growth model used to simulate the formation and evolution of the SEI layer in lithium-ion batteries. SEI layer forms on the negative electrode and as its thickness increases it will opposes the conductivity between electrode and electrolyte. To replicate this behaviour in PyBaMM solvent diffusion limited is chosen. The term "solvent-diffusion limited" indicates that the growth of the SEI layer is primarily controlled by the diffusion of solvent molecule from the electrolyte solution towards the electrode surface. As these solvent molecules diffuse to the surface, they react with the electrolyte salts to form the SEI layer. The rate of SEI growth in this model is limited by the rate of solvent diffusion and cycling conditions.

As the SEI growth on the electrode increase it will lead to an increase in the internal resistance for ions to transport between electrolyte and electrode. It also reduce the effective active surface on the electrode for electrochemical reaction which will lead to reduce in lithium intercalate and deintercalate during charge and discharge cycles in electrode, resulting in a loss of battery capacity [2]. Additionally as the SEI layer growth increases it traps lithium ions within the layer leading to reduction in active available lithium leading to loss of lithium inventory (LLI).

"Loss of active material(LAM): stress and reaction-driven" is one of the degradation mechanisms for LAM for both cathode and anode in PyBaMM due to the mechanical stress generated in the electrode and reaction driven which is caused by a combination of side reactions[36], electrolyte decomposition, and SEI formation [37].

Repetitive charging and discharge cycling lead to loss of active material in the electrodes due to repetitive lithation and dilithiation causing the electrodes to undergo volume expansion and contraction, which induce mechanical fatigue and structural degradation over time. This cyclic stress can also weaken the bonds between active material particles and the current collector, resulting in particle detachment and loss of active material.

Listing 4.2: Model setup for aging.

```
%% Okane2022 parameter set is chosen. %%
param = pybamm.ParameterValues("OKane2022")

%% DFN Model along with Degradation mechanism chosen. %%
model = pybamm.lithium_ion.DFN(options={
"SEI": "solvent-diffusion limited",
"loss of active material": "stress and reaction-driven",
            })

%% Modifying the default cell parameters. %%
param.update({
"Outer SEI solvent diffusivity [m2.s-1]":1.25e-22,
"Positive electrode LAM constant proportional term [s-1]":1e-2
"Negative electrode LAM constant proportional term [s-1]":1e-2
            })
```

Listing 4.2 illustrates the implementation of the degradation mechanisms in PyBaMM. To age a cell in PyBaMM, the user must clearly specify the type of degradation mechanism in the model options, as shown in Listing 4.2. Following this, the cell must be cycled as explained in Listing 4.1. The cell ages more as the number of cycles increases.

To accelerate the aging process, one can modify the standard cycling protocol. Charging and discharging at higher rates were found to accelerate the cell degradation. Similarly, to target specific parts of the cell for faster aging compared to other degradation modes, modifying the cell's default parameters can also yield such results. For example, changing the value of the "Outer SEI solvent diffusivity $[m^2 s^{-1}]$" parameter would trigger a faster loss of lithium inventory compared to LA) for the anode and cathode.

All the different experiment types discussed previously were performed, and the data was stored for testing and developing degradation mode estimation algorithms. In the first case, by specifying only the degradation mechanism and using the standard cycling protocol, we observe standard cell aging. In the next setup, we create a scenario where the cell is charged or discharged at higher speeds, resulting in faster degradation compared to the previous setup. In another setup, we simulate a scenario where a particular degradation mode shows a faster trend compared to the others. This could occur due to shorting of the electrode or loss of a certain amount of material. To create such rare scenarios, default cell parameters can be modified. To accelerate this process, it can also be coupled with the second setup by modifying the charge and discharge rates.

4.2.3 Data Collection

This section discusses the data collection process and the steps involved. The estimation algorithm requires OCV vs SOC data as input to estimate degradation modes such as LLI, LAM_{PE} and LAM_{NE}. To verify the estimated degradation modes, the values calculated by PyBaMM are stored as ground truth. Additionally, data on cell aging, including capacity and the number of cycles, is collected to understand the trend and behavior of the cell.

Fig. 4.7 illustrates how the cell is cycled in PyBaMM using a standard cycling protocol method as described in Listing 4.1. The first 10 oscillations in the cell voltage versus time curve show the charge and discharge phases. Subsequently, after resting the cell, a pulsating discharge load is applied, as depicted in the zoomed section of the current versus time graph. This load application leads to a drop in voltage, as shown in the zoomed section of the cell voltage versus time graph. Once the load is removed, the battery is allowed to relax or rest, and at the end of the rest phase, an OCV point is collected, indicated by the red point in Fig. 4.7.

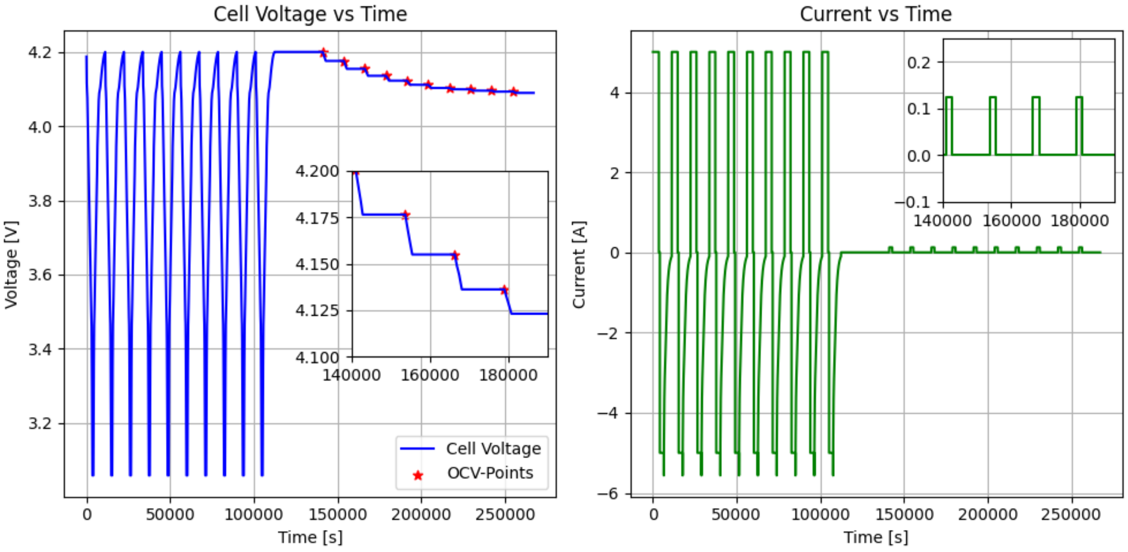

Figure 4.7: Standard Cycling & OCV-Point collection

To plot OCV points, SOC data is required, which cannot be extracted directly from PyBaMM. To calculate the SOC, the Coulomb counting method was implemented. The basic principle behind Coulomb counting [38] is tracking the amount of charge flowing in and out of the battery over time and integrating it continuously, according to,

$$SOC(t) = SOC(t_o) + \frac{1}{C_n} \int_{t_o}^{t} I(\tau) d\tau \tag{4.4}$$

Where, SOC(t) represents the state of charge at time t, SOC(t_0) represents the initial state of charge at time t_0, C_n is the nominal cell capacity (Ah), and $I(\tau)$ represents the current flowing in and out of the cell at time τ. This method calculates the SOC of the cell in terms of capacity, which means that when integrating the current from fully charged to discharged states, we get the total amount of charge the cell can hold. Over time, this capacity reduces. By dividing this integrated current by the nominal capacity of the cell, we obtain the SOC in terms of capacity.

In this work, SOC is represented in terms of voltage. This means that whenever the cell voltage is measured to be 4.2 V, it corresponds to 1% SOC, and when the cell voltage is 3.3 V, it corresponds to 0% SOC. This method is being followed in Volvo Cars, so the same method has been adopted for the current work. To implement SOC in the voltage method, first, after completing the experiment, the pulsating discharge current data is extracted from PyBaMM. Then, the pulsating discharge current data is filtered to include only the current data when the cell voltage is between 4.2 and 3.3 Volts. Now, the filtered current data is integrated and divided by 3600 to obtain the capacity of the cell in Ah, known as the updated cell capacity, which changes after every usage of the cell. Eq. (4.4) is modified by replacing the nominal capacity with the updated cell capacity, denoted as C_{update}. The equation is updated and rewritten as,

$$SOC(t) = SOC(t_o) + \frac{1}{C_{update}} \int_{t_o}^{t} I(\tau) d\tau \tag{4.5}$$

In Fig. 4.8, the comparison of how the OCV curve data of the same age cell can be represented using Voltage SOC and Capacity SOC methods is shown. In the figure, the "Open-Circuit Voltage" curve is plotted using the Voltage SOC method, where 4.2 V represents 100% SOC and 3.3 V represents 0% SOC. In contrast, the "Open-Circuit Voltage capacity" curve is plotted using the Capacity SOC method, where the cutoff voltage, 2.6 V, is reached when the SOC value is less than 0.1%.

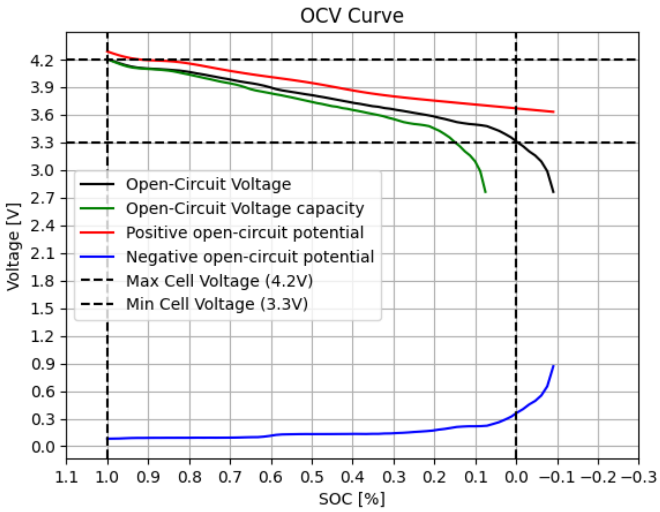

Figure 4.8: Comparison between voltage SOC & capacity SOC.

Fig. 4.9 illustrates the degradation modes vs throughput capacity, which is extracted from PyBaMM. Throughput capacity represents the cumulative charge-discharge the battery has undergone during the cycling process. The graph demonstrates how degradation modes increase as the cell undergoes the cycling. At the end of the cycling, degradation values were stored as ground truth.

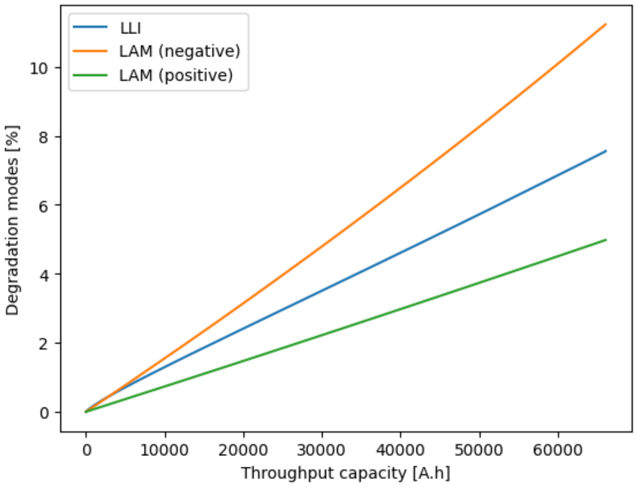

Figure 4.9: Degradation modes sample curve.

4.3 OCV Curve Comparison

Figure 4.10 depicts a comparison between different aged cells and a pristine cell, which have been collected by performing various cycling simulations in PyBaMM. As can be seen in Fig. 4.10,

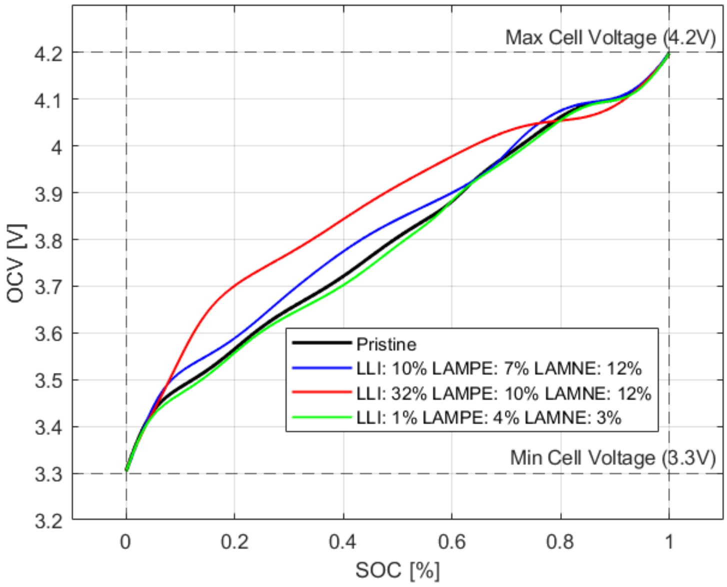

Figure 4.10: OCV comparison of different aged cells.

5

Methodology

This chapter synthesizes the information presented in previous chapters to explore the impact of degradation mechanisms on specific degradation modes within batteries. These degradation modes are not directly observable through the physical characteristics of the battery but can be inferred from voltage measurements. Based on experimental research [20][4][2][39], a correlation between degradation modes and OCP curves has been established. This chapter delves into how these degradation modes manifest as changes in the OCP curves and discusses the extent to which these changes reflect the severity of the degradation.

By analyzing the alterations in the OCP curves, it is possible to develop an algorithm capable of leveraging these changes to estimate the degradation modes accurately. This algorithm can provide valuable insights into the battery's health and predict its performance over time. The chapter outlines the methodology for deriving this algorithm and validates its efficacy through experimental data, emphasizing its potential applications in battery management systems for enhanced monitoring and maintenance.

5.1 Theory

In lithium-ion batteries, lithium ions migrate between the positive electrode (cathode) and the negative electrode (anode) during operation. When the battery is being charged, lithium ions move from the positive electrode to the negative electrode, resulting in an increase in the normalized lithium concentration in the negative electrode (x_{NE}). Concurrently, the normalized lithium concentration in the positive electrode (x_{PE}) decreases. During the discharging process, the opposite occurs: lithium ions travel back to the positive electrode, increasing x_{PE} and decreasing x_{NE}.

A crucial assumption in this analysis is that the relationships between the open-circuit potential (OCP) and the state of charge (SOC) for both electrodes—specifically, $OCP_{NE} - SOC_{NE}$ and $OCP_{PE} - SOC_{PE}$—remain invariant throughout the battery life-time. This assumption has been validated through extensive practical experiments and is supported by empirical evidence in the literature [40][6].

The OCPs for the electrodes have been derived analytically using theoretical logarithmic terms that align with the Butler-Volmer equation, which describes the kinetics of electrochemical reactions [41][16][42]. There are multiple methodologies for deriving OCP curves, including polynomial approximations, ECMs, and impedance-dependent models [43]. Each approach offers different advantages in terms of accuracy, computational complexity, and applicability to various battery conditions.

For the purposes of this work, we utilize the OCP model parameterized by Chen *et al.* [4]. This model provides as accurate representation of the OCP behavior in NMC cells. The general functions for the OCP curves are expressed as:

$$\begin{aligned} OCP_{NE} &= f_{NE}(SOC_{NE}) \\ OCP_{PE} &= f_{PE}(SOC_{PE}) \end{aligned} \tag{5.1}$$

where f_{NE} and f_{PE} are the functional relationships derived from empirical and theoretical data that describe the OCP as a function of the SOC for the negative and positive electrodes, respectively.

Here, the OCP values is replaced with U_x (x = PE, NE) to represent the voltage values and SOC is replaced with x_x, the stoichiometric coefficients. Stoichiometric coefficients refers to a normal concentration/amount of lithium present in the electrode. It ranges between 0 and 1, where 0 corresponds to the electrode being completely delithiated and 1 corresponds to a fully lithiated electrode. Eq.(5.1) can then be re-written as,

$$\begin{aligned} U_{NE} &= f_{NE}(x_{NE}) \\ U_{PE} &= f_{PE}(x_{PE}) \end{aligned} \tag{5.2}$$

where U_{NE} and U_{PE} are as mentioned in eq.(4.3) and eq.(4.2).

Using the eq.(4.2) and eq.(4.3), we can analyze the effects of the degradation modes, LAM_{PE}, LAM_{NE} and LLI.

5.1.1 LAM_{PE}

When battery degradation is solely due to the loss of active material in the positive electrode (denoted as LAM_{PE}), the open-circuit potential (OCP) curve of the negative electrode (NE) remains unaffected. However, for the positive electrode (PE), the OCP curve exhibits a distinct change: the endpoint corresponding to a normalized lithium concentration of zero remains fixed, while the rest of the curve contracts from the left side. This contraction occurs in a proportion directly corresponding to the extent of LAM_{PE} (see Fig. 5.1a) [20].

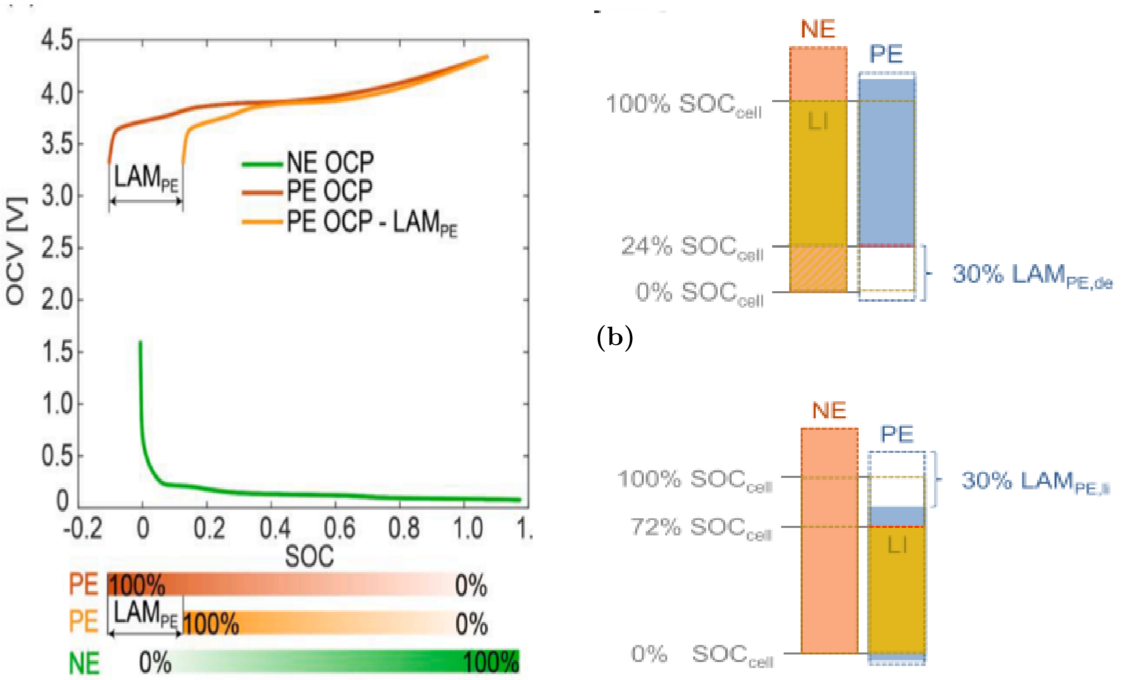

(a)

(b)

(c)

Figure 5.1: Loss of active material in the positive electrode. (a) Proportional scaling of the OCP of the positive electrode due to LAM [20] (b) Change in concentrations of lithium and electrode material in case of LAM while the positive electrode is delithiated [7] (c) Change in concentrations of lithium and electrode material in case of LAM while the positive electrode is lithiated [7]

Fig. 5.1b and Fig. 5.1c show how the affect is on the electrode materials and lithium concentrations in the cell along with the corresponding SOC/stoichiometric coefficients. Loss of active material of the positive electrode takes place with and without lithium inventory in it respectively.

5.1.2 LAM_{NE}

When the degradation of the battery is exclusively due to the loss of active material in the negative electrode (denoted as LAM_{NE}). Conversely, the OCP curve of the negative electrode (NE) shows a specific alteration: the endpoint corresponding to a normalized lithium concentration of zero remains fixed, while the curve contracts from the right side. This shrinkage from the right occurs in proportion to the degree of LAM_{NE} (see Fig. 5.2a) [20].

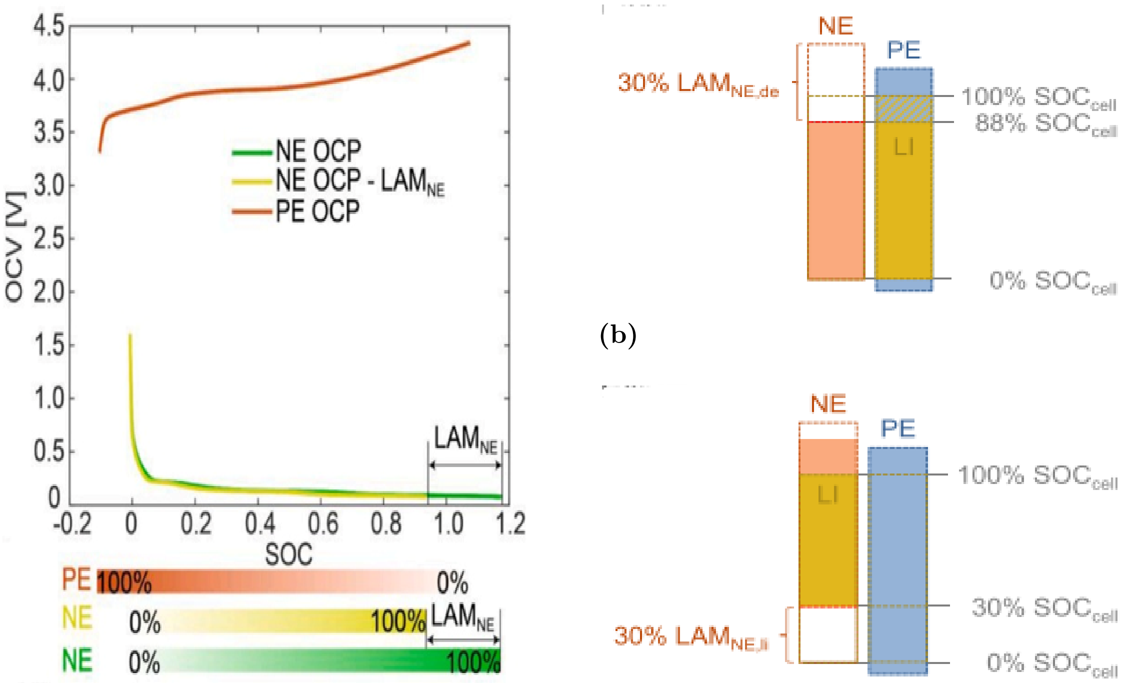

(a) (b) (c)

Figure 5.2: Loss of active material in the negative electrode. (a) Proportional scaling of the OCP of the negative electrode due to LAM [20] (b) Change in concentrations of lithium and electrode material in case of LAM while the negative electrode is delithiated [7] (c) Change in concentrations of lithium and electrode material in case of LAM while the negative electrode is lithiated [7]

Fig. 5.2b and Fig. 5.2c present data on the concentrations of electrode materials and lithium within the cell, along with the associated state of charge (SOC) and stoichiometric coefficients. These figures illustrate the change in concentration profiles that occur due to the loss of active material in the negative electrode, both in the presence and absence of lithium inventory.

5.1.3 LLI

When the battery degradation path is exclusively due to the loss of lithium inventory (LLI), the open-circuit potential (OCP) curve of the positive electrode remains unchanged in both its position and shape. In contrast, the OCP curve of the negative electrode (NE) does not exhibit any reduction in its span or shape; instead, it translates horizontally to the right along the voltage axis.

This rightward translation of the NE OCP curve is a direct reflection of the degree of lithium inventory loss. The shift occurs because LLI results in a decrease in the overall lithium available for intercalation and deintercalation processes within the electrode. Consequently, for a given state of charge (SOC), the lithium concentration in the NE becomes higher compared to a fresh cell with intact lithium inventory, leading to the observed rightward shift in the OCP curve.

The degree of this translation is proportional to the extent of LLI, meaning that a greater loss of lithium inventory will result in a more significant rightward shift of the NE OCP curve. This relationship provides a clear and quantifiable measure of LLI within the cell. By analyzing the amount of translation, one can infer the extent of lithium inventory degradation.

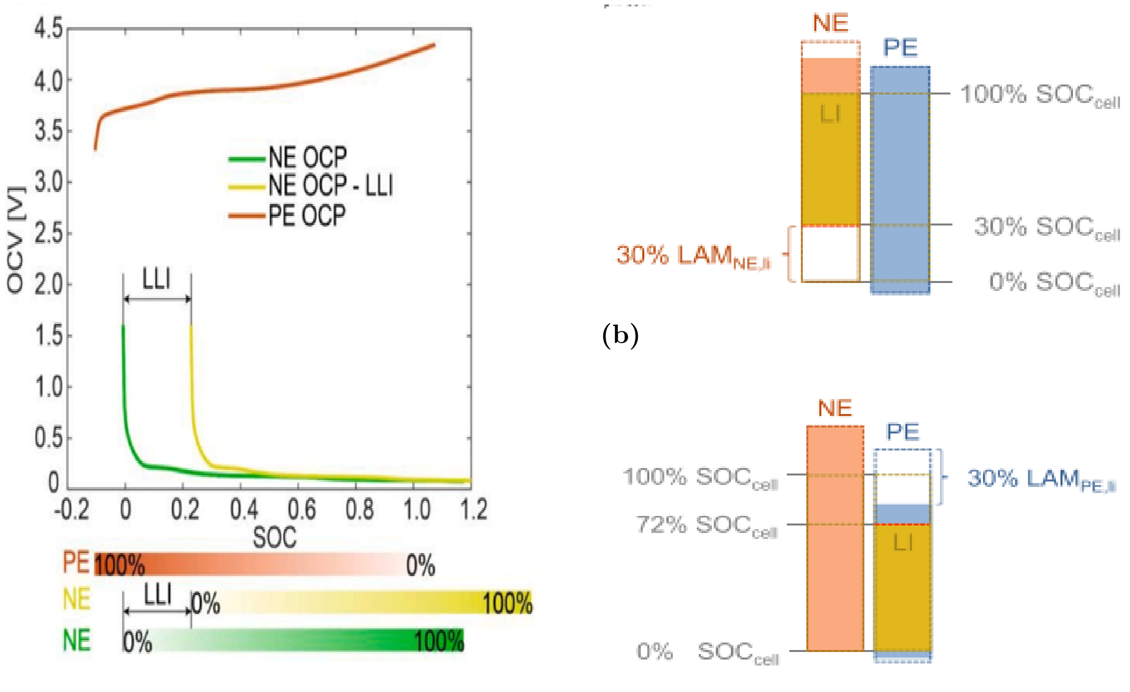

(a)

(b)

(c)

Figure 5.3: Loss of lithium inventory (a) Proportional shifting of the OCP of the negative electrode due to LLI [20] (b) Change in concentrations of lithium while the negative electrode is lithiated [7] (c) Change in concentrations of lithium while the positive electrode is lithiated [7]

Fig. 5.3a demonstrates how the shifting of OCP_{NE} is proportional to the degradation of the positive electrode. Fig. 5.3b and Fig. 5.3c present data on the concentrations of electrode materials and lithium within the cell, along with the associated state of charge (SOC) and stoichiometric coefficients. These figures illustrate the shifts in concentration profiles that occur due to the loss of lithium inventory in the positive and negative electrode, in the presence of lithium inventory.

5.2 Algorithm

Using the information from the previous sections, an algorithm can be developed to estimate the degree of each of the degradation modes. This algorithm is divided into 2 main parts, Calibration and Estimation.

5.2.1 Calibration

The P2D model, incorporating the parameter sets from Chen *et al* [4]. and the modifications by O'Kane *et al* [2], allows for realistic simulations of LG M50 cells, taking into account various physical and chemical phenomena, such as ion transport, electrochemical reactions, and thermal effects.

Schmitt *et al* [18] describes the relation between the OCP curves and the OCV curve of the full cell. This is described as,

$$U_{full}(x_{full}) = U_{PE}(x_{PE}) - U_{NE}(x_{NE}) \tag{5.3}$$

where U_{NE} and U_{PE} are mentioned as eq.(4.3) and eq.(4.2) .Schmitt *et al* also show how any OCV curve can be described using the OCP curves. By introducing scaling (α_{PE}, α_{NE}) parameters and shifting (β_{PE}, β_{NE}) parameters for the cathode and anode, respectively the cell SOC can be expressed as,

$$x_{full} = \alpha_{NE} \cdot x_{NE} + \beta_{NE} \tag{5.4}$$

$$x_{full} = \alpha_{PE} \cdot x_{PE} + \beta_{PE} \tag{5.5}$$

which can be rewritten as

$$x_{NE} = \frac{x_{full} - \beta_{NE}}{\alpha_{NE}} \tag{5.6}$$

$$x_{PE} = \frac{x_{full} - \beta_{PE}}{\alpha_{PE}} \tag{5.7}$$

Thus, inserting eq.(5.6) and eq.(5.7) in eq.(5.3), we get

$$U_{full} = U_{PE}(\frac{x_{full} - \beta_{PE}}{\alpha_{PE}}) - U_{NE}(\frac{x_{full} - \beta_{NE}}{\alpha_{NE}}) \tag{5.8}$$

Chen *et al* [20] describes a methodology to reconstruct OCV curve graph. This can be used for reconstructing an aged/ degraded cell's OCV curve.

Using the method by Schmitt *et al* method [18], the pristine cell OCV is first fitted to the OCP curves according to

$$\begin{aligned} x_{full} &= \alpha_{NE} \cdot x_{NE} + \beta_{NE} \\ &= \alpha_{NE} \cdot f_{NE}^{-1}(U_{NE}) + \beta_{NE} \end{aligned} \tag{5.9}$$

$$\begin{aligned} x_{full} &= \alpha_{PE} \cdot x_{PE} + \beta_{PE} \\ &= \alpha_{PE} \cdot f_{PE}^{-1}(U_{PE}) + \beta_{PE} \end{aligned} \tag{5.10}$$

to get α and β for the pristine cell. The scaling and shifting coefficients for the pristine cell [$\alpha_{PE,pris}$, $\alpha_{NE,pris}$, $\beta_{PE,pris}$, $\beta_{NE,pris}$] can be determined by solving the optimization problem

$$\theta_m = argmin_{\theta_m} \sqrt{\frac{1}{N}\sum_{i=1}^{N}(OCV_i - (U_{PE,i} - U_{NE,i}))^2} \tag{5.11}$$

where 'N' is the total number of sample points of the OCV curve and
$\theta_m = [\ \alpha_{PE,pris},\ \beta_{PE,pris},\ \alpha_{NE,pris},\ \beta_{NE,pris}\ ]$.

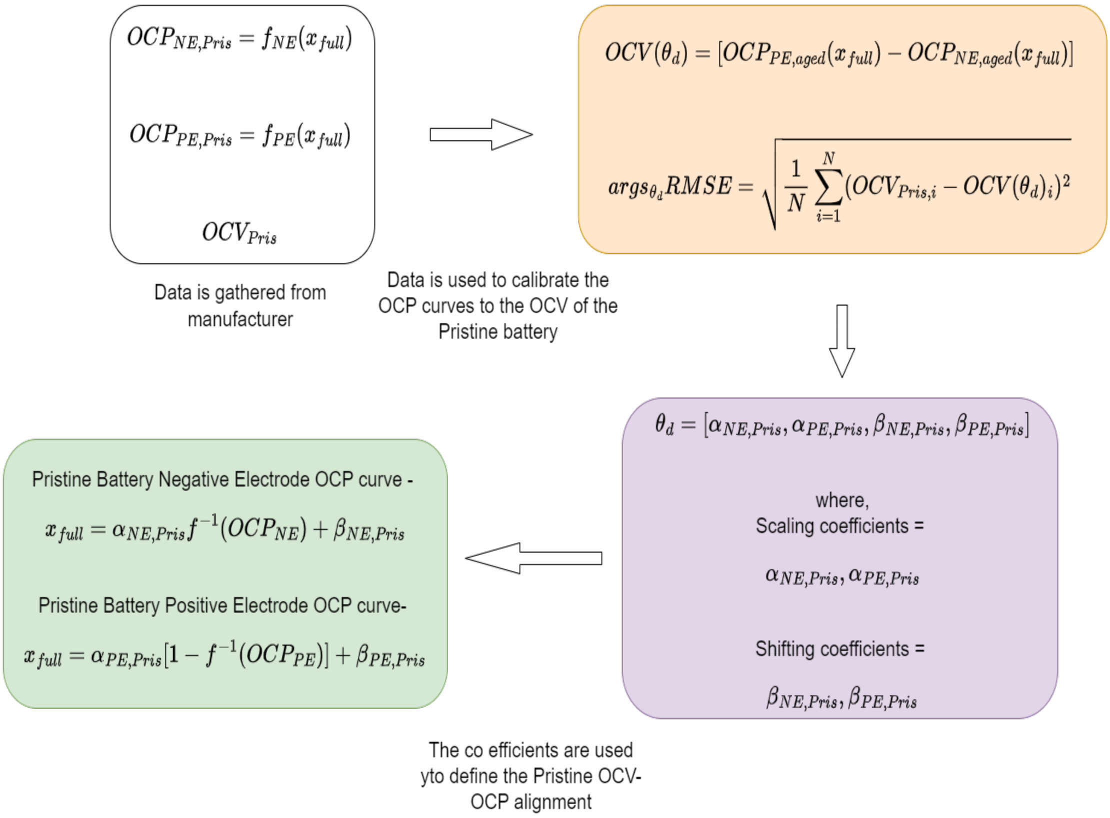

Figure 5.4: Flowchart of the calibration algorithm

Fig. 5.4 summarizes the calibration process as mentioned above.

5.2.2 Estimation

Now, by understanding the effects of various degradations upon the OCP curves, the aged OCP curves can be determined and thereby the aged OCV curve.

Effect of LAM_{NE} is a scaling effect on the OCP_{NE}:

$$x_{full} = \alpha_{NE,pris} \cdot (1 - LAM_{NE}) \cdot f_{NE}^{-1}(U_{NE}) + \beta_{NE,pris} \tag{5.12}$$

Effect of LAM_{PE} is a scaling effect on the OCP_{PE}:

$$x_{full} = \alpha_{PE,pris} \cdot [1 - (1 - LAM_{PE}) \cdot f_{PE}^{-1}(U_{PE})] + \beta_{PE,pris} \tag{5.13}$$

Effect of LLI is a shifting effect on the OCP_{NE}:

$$x_{full} = \alpha_{NE,pris} \cdot f_{NE}^{-1}(U_{NE}) + \beta_{NE,pris} + LLI \tag{5.14}$$

Thus, the OCP curves can be defined for any degradation by specifying the degradation modes' degree.

$$\begin{aligned} x_{full} &= \alpha_{NE,pris} \cdot (1 - LAM_{NE}) \cdot f_{NE}^{-1}(U_{NE}) + \beta_{NE,pris} + LLI \\ x_{full} &= \alpha_{PE,pris} \cdot [1 - (1 - LAM_{PE}) \cdot f_{PE}^{-1}(U_{PE})] + \beta_{PE,pris} \end{aligned} \tag{5.15}$$

This can be re-written as,

$$U_{NE}(x_{full})_{aged} = f_{NE}\left[\frac{x_{full} - LLI - \beta_{NE,pris}}{\alpha_{NE,pris}(1 - LAM_{NE})}\right] \tag{5.16}$$

$$U_{PE}(x_{full})_{aged} = f_{PE}\left[\frac{1 - \left[\frac{x_{full} - \beta_{PE,pris}}{\alpha_{PE,pris}}\right]}{1 - LAM_{PE}}\right] \tag{5.17}$$

Thus,

$$OCV[X_{full}]_{aged} = U_{PE}(x_{full})_{aged} - U_{NE}(x_{full})_{aged} \tag{5.18}$$

By following on the lines of Birkl *et al* [7], the degradation modes [*LLI*, LAM_{PE}, LAM_{NE}] can be used as parameters to fit onto the OCV of an aged cell,

$$\theta_d = argmin_{\theta_d}\sqrt{\frac{1}{N}\sum_{i=1}^{N}(OCV(\theta_d)_i - OCV_{meas,i})^2} \tag{5.19}$$

where 'N' is the total number of sample points of the OCV/ OCP curve and
$\theta_d = [\ LLI,\ LAM_{PE},\ LAM_{NE}\ ]$.

Thus, convergence to a true minimum of eq.(5.19) should provide the degradation modes 'θ_d' from the measured OCV. Fig. 5.5 summarizes this estimation process.

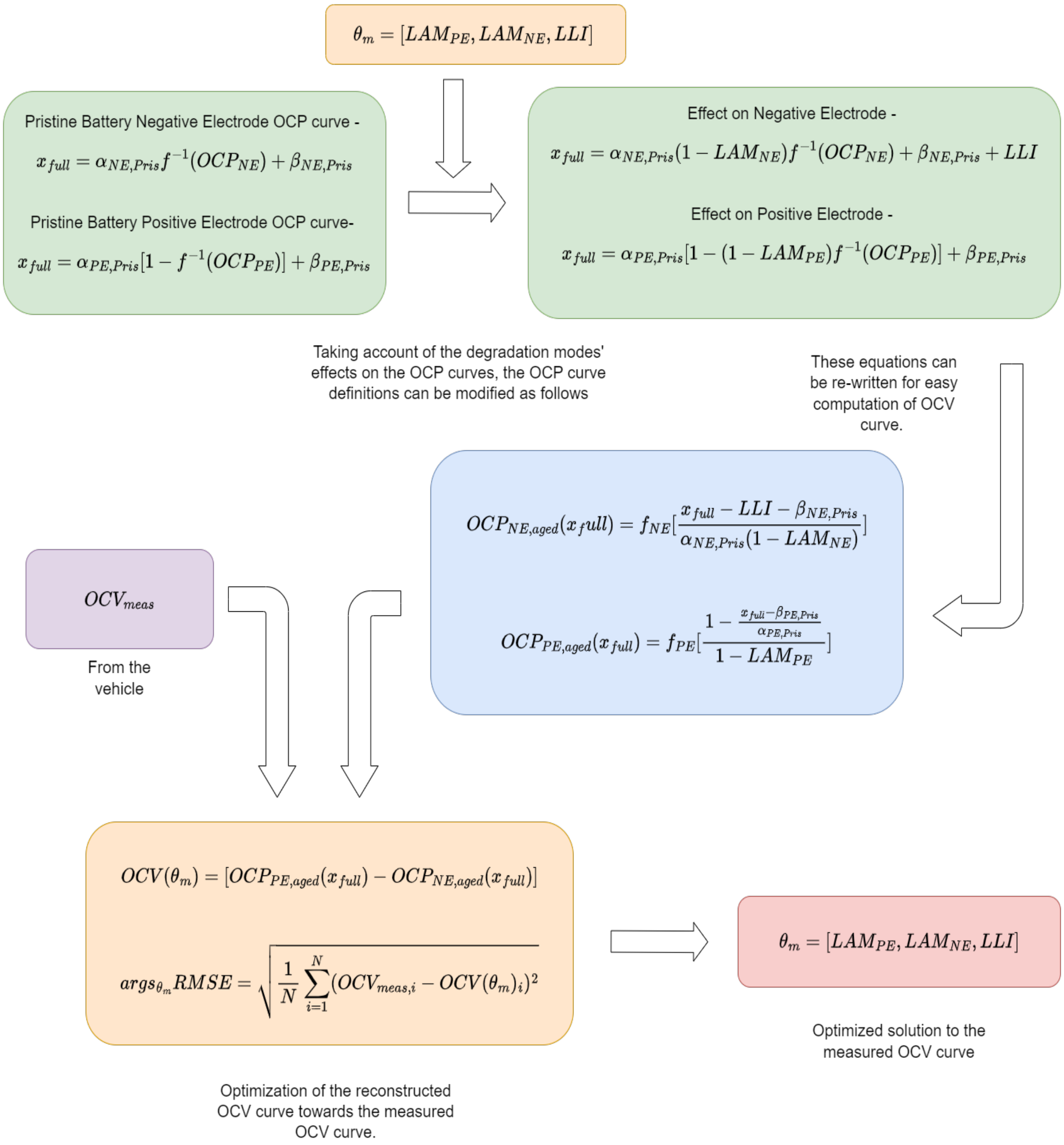

Figure 5.5: Flowchart of the Estimation algorithm

6

Results and Discussions

As cells age, their behavior changes, which we can study by analyzing their OCV curves. This curve undergoes shifts over time, offering a valuable window to understand the degradation modes within the cell. Leveraging these shifts, algorithms have been developed to estimate degradation modes. In this section we first assess accuracy of these reconstructions compared to the actual OCV curve then subsequently efficacy of algorithms in capturing degradation modes by reconstructing the OCV curve.

6.1 Reconstruction of OCV(ROCV)

In the previous chapter, it was discussed that aging a cell through PyBaMM is a time-consuming process, as the simulation needs to run for a large number of cycles to adequately age the cell. To reduce simulation time, an algorithm was developed that takes degradation mode values as input and generates the OCV curve. In this section, the focus will be on verifying and evaluating how closely the algorithm-generated OCV curve matches the PyBaMM-generated curve, which is considered the ground truth. This comparison will help determine the algorithm's accuracy and effectiveness in replicating the aging process.

In Fig. 6.1, cell data collected from PyBaMM after 1500 cycles is presented, showing degradation mode values of LLI: 1.84%, LAM_{PE}: 1.08%, and LAM_{NE}: 2.3%. These degradation values were provided as input to the algorithm, and the resulting OCV curve was reconstructed, as shown in Fig. 6.1. It is evident that the algorithm-generated curve closely tracks the PyBaMM curve. The root mean square error (RMSE) value is in the order of 10^{-3}, indicating that the algorithm can quite accurately recreate the PyBaMM OCV curve.

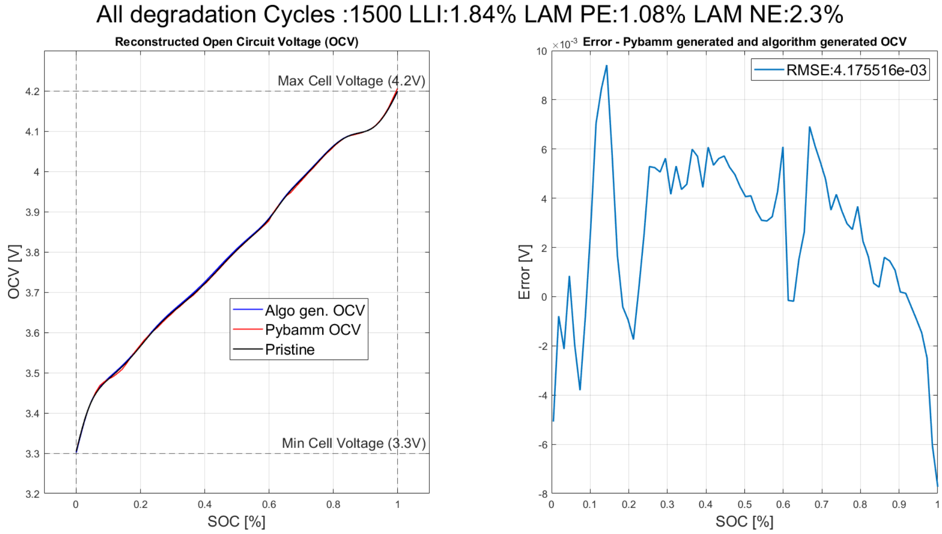

Figure 6.1: ROCV cell cycled:1500 LLI:1.84% LAM_{PE}:1.08% LAM_{NE}:2.3%.

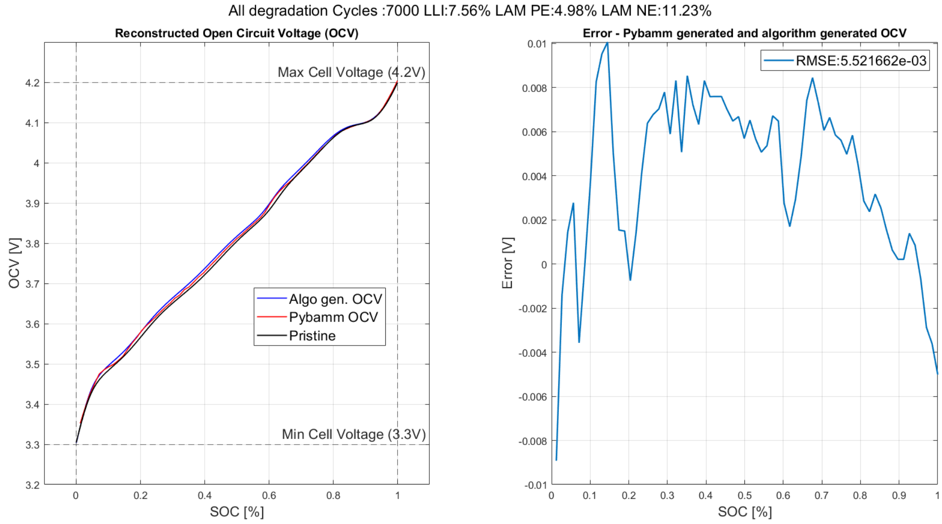

Figure 6.2: ROCV cell cycled:7000 LLI:7.56% LAM_{PE}:4.98% LAM_{NE}:11.23%.

Referring to Fig. 6.1, 6.2, and 6.3, it is evident that in all three cases, the RMSE value is in the order of 10^{-3}, indicating that the estimations are relatively accurate. One peculiar behavior observed in all three cases is that the error value is higher in the SOC range of 0.1 to 0.2, as shown in the error graphs. This leads to a deviation in the reconstructed OCV curve from the actual PyBaMM curve. The next set of verification tests will be conducted to understand if this deviation affects the estimation of the degradation modes.

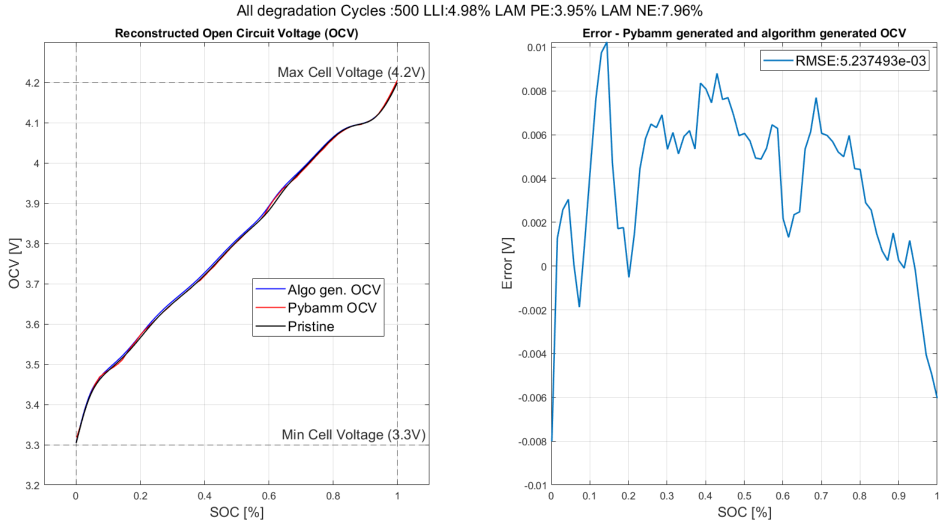

Figure 6.3: ROCV cell cycled:500 LLI:4.98% LAM_{PE}:3.95% LAM_{NE}:7.96%.

6.2 Validation

In this section, the algorithm's validation and verification are carried out through testing on differently aged cells for different scenario. Four datasets have been carefully selected to present and explain the results. These datasets are chosen to cover a spectrum of degradation modes, ranging from 0 to 10%, 10 to 20%, and 20 to 30% and beyond. Moreover, efforts were made to include situations where certain degradation modes exhibited abnormal degradation patterns. Through this comprehensive dataset selection, the aim is to evaluate the algorithm's performance across various aging scenario.

6.2.1 Continuous data

In this experiment, a continuously sampled OCV curve data is fed into the algorithm to predict the degradation modes. Fig. 6.4 shows how the algorithm perfectly tracks the OCV curve, with the estimated degradation mode values matching the ground truth. However, this isn't the case for all scenarios due to the non-convex nature of the problem, which means multiple local minima exist. Different combinations of degradation mode values can produce similar OCV curves, which might fit the ground truth OCV curve nearly.

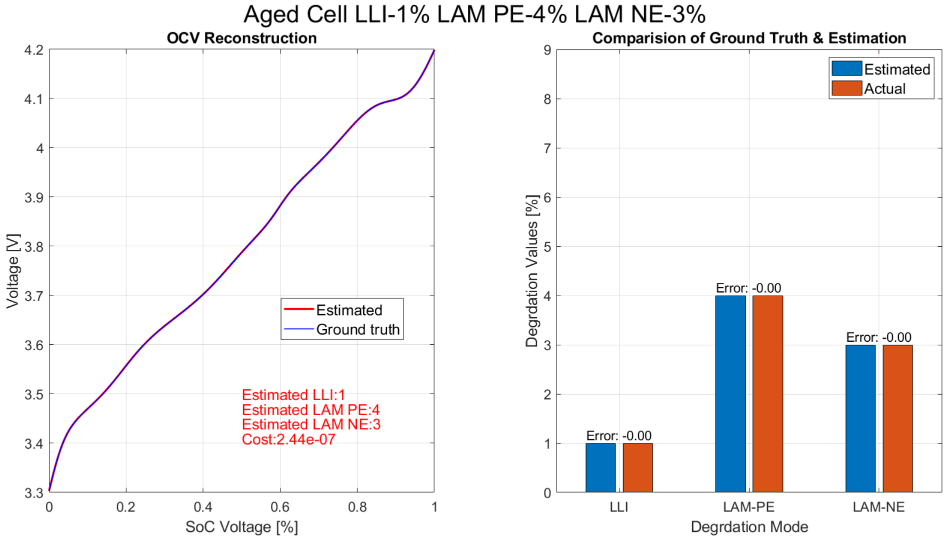

Figure 6.4: Continues data: Aged cell LLI:1% LAM_{PE}:4% LAM_{NE}:3%.

Fig. 6.5 illustrates why the optimization problem is non-convex. In this example, one of the degradation mode parameters is fixed to its ground truth value, while the other two parameters are varied to observe how the cost value changes. With the LAM_{NE} value locked[1], the graph clearly shows that the lowest cost value lies in the region of 0% to 0.1% for both LLI and LAM_{PE}. When zooming into this region, multiple valleys with very similar cost values are observed.

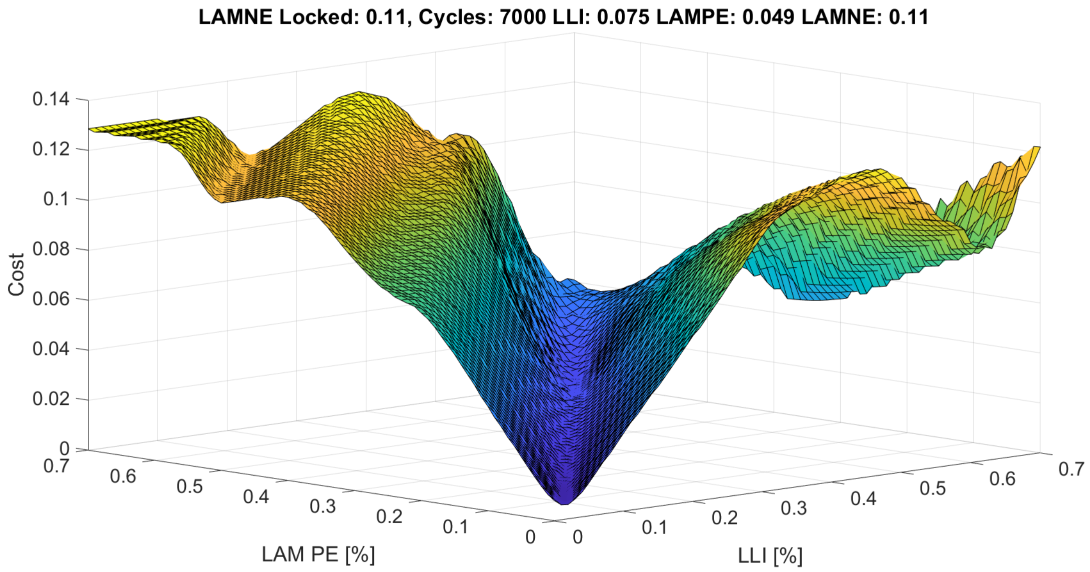

Figure 6.5: Cost graph: Cycled 7000 LLI:7.56% LAM_{PE}:4.98% LAM_{NE}:11.23%

In Table 6.1, the results of seven test cases evaluating the convexity of the problem are presented. The first three cases, namely Free-reg 1, Free-reg 2, and Free-reg 3,

---

[1] Similar cost graphs are mentioned in the appendix, where other parameters are fixed and varied.

were conducted without applying any constraints. The fourth and fifth cases, referred to as Constraint-reg 1 and Constraint-reg 2, incorporated specific constraints during the testing. Finally, in the sixth and seventh cases, labeled Constraint-reg+AVG 1 and Constraint-reg+AVG 2, the optimizer was executed 30 times, and the average values from these runs were recorded.

To explain this further, the same cell sample was tested under different conditions, as shown in Table 6.1. It was clearly observed that when the lower bound (LB) and upper bound (UB) were left unconstrained or given a larger search region, the estimated values deviated significantly from the ground truth, despite having a very low cost value. This deviation occurred because multiple local minima existed, leading the optimizer to converge on different combinations of degradation mode values that could produce similar OCV curves. As illustrated in Fig. 6.6, these different combinations might fit the ground truth OCV curve perfectly.

To mitigate this issue and improve estimation accuracy, constraints were applied to the degradation modes, as discussed in the methodology section. This approach reduced the search region for the optimization parameters, thereby improving the estimation, as shown in Table 6.1. Additionally, running the optimization 30 times and averaging the results provided a more reliable estimation.

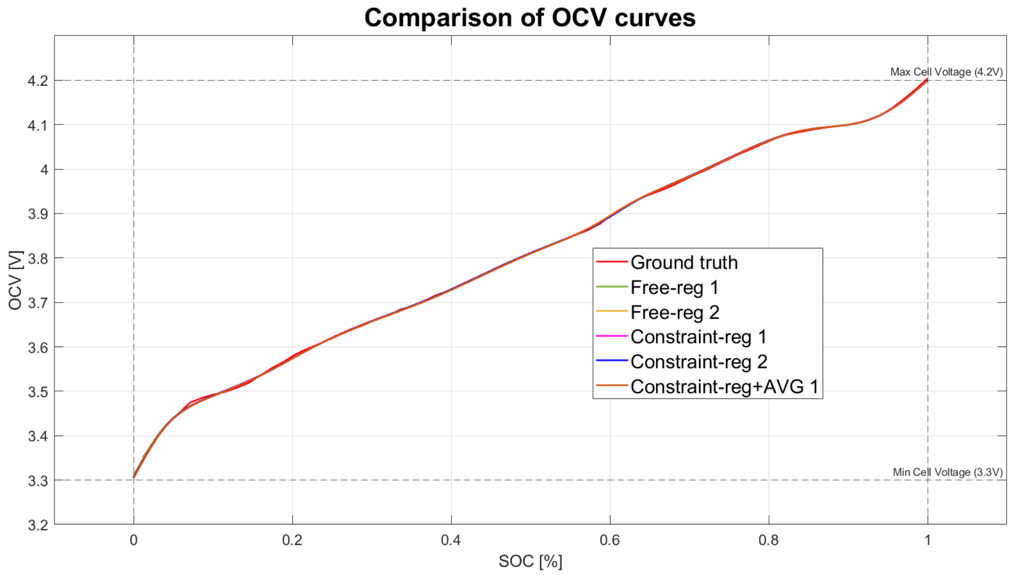

Figure 6.6: OCV Comparison.

Fig. 6.7, 6.8, 6.9 illustrates that the estimation algorithm perfectly tracks the ground truth OCV curve with errors less than ±2%.

Table 6.1: Checking the convexity of the problem.

Aged Cell Cycled: 7000 Ground truth: [LLI: 7.56 LAM_{PE}: 4.98 LAM_{NE}: 11.23]			
Condition	[LB, UB]	Estimated Deg	Cost
Free-reg 1	[0,70]	[9.2, 6.68, 12.85]	7.62×10^{-5}
Free-reg 2	[0,70]	[36.4, 35.2, 39.5]	1.20×10^{-5}
Free-reg 3	[0,70]	[21.5, 19.6, 24.8]	2.32×10^{-5}
Constraint-reg 1	[0,16]	[3.75, 0.98, 7.41]	1.09×10^{-5}
Constraint-reg 2	[0,16]	[10.72, 8.30, 14.32]	2.13×10^{-5}
Constraint-reg+AVG 1	[0,16]	[7.41, 4.91, 11.41]	3.54×10^{-4}
Constraint-reg+AVG 2	[0,16]	[8.74, 6.37, 13.03]	6.80×10^{-4}

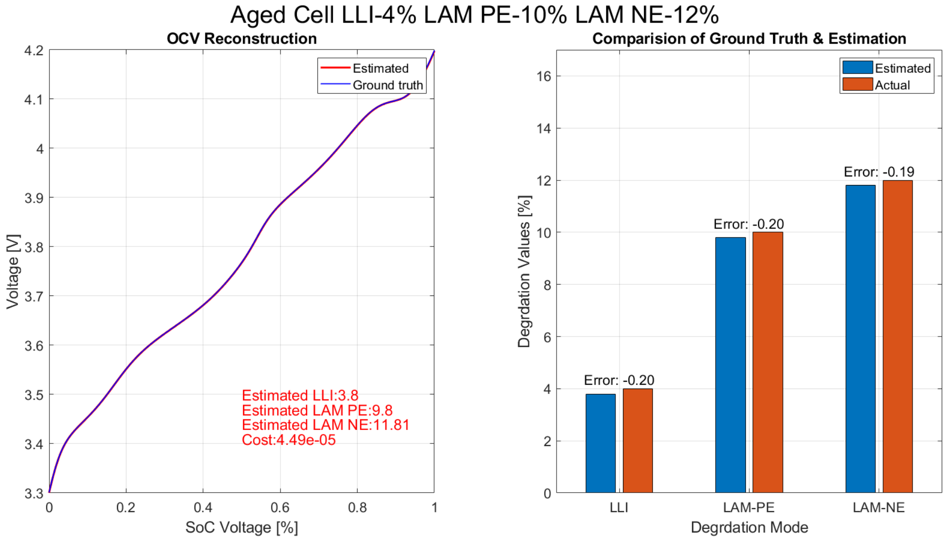

Figure 6.7: Continues data: Aged cell LLI:4% LAM_{PE}:10% LAM_{NE}:12%.

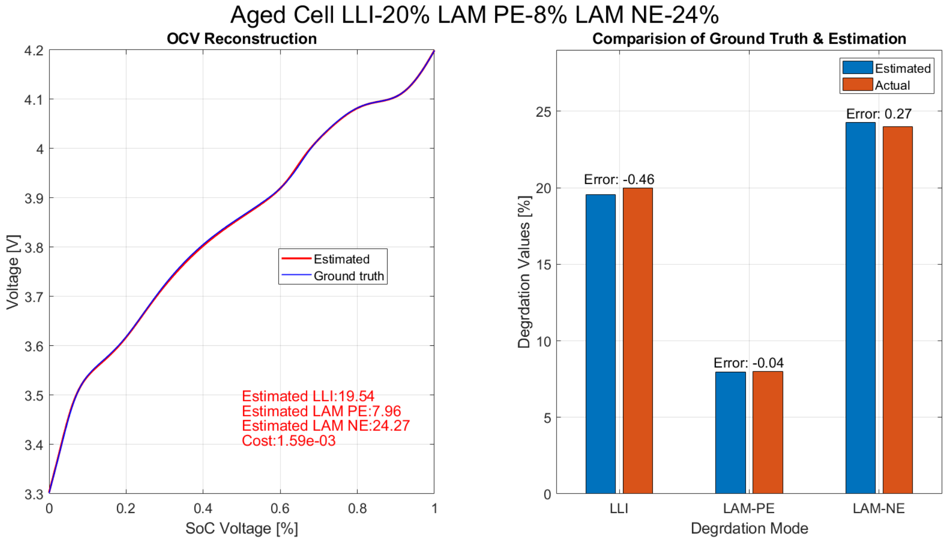

Figure 6.8: Continues data: Aged cell LLI:20% LAM_{PE}:8% LAM_{NE}:24%.

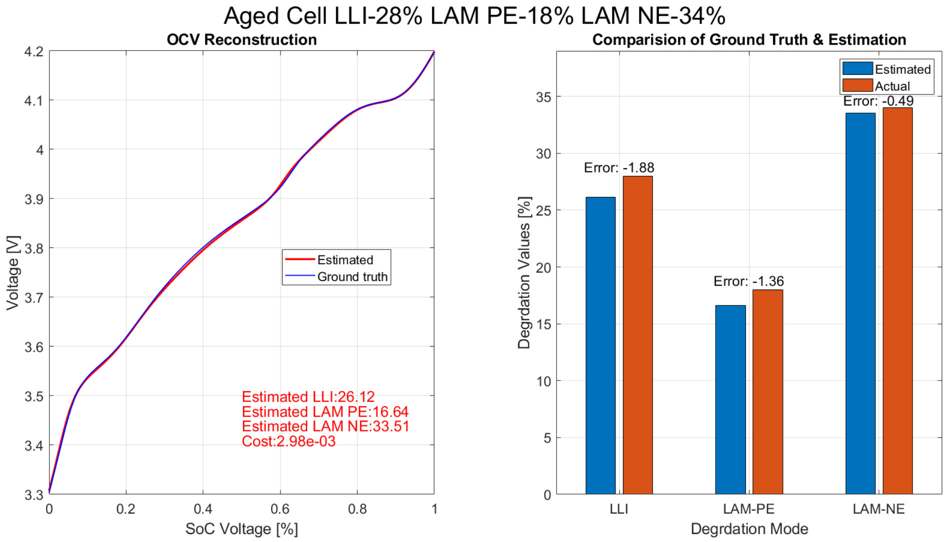

Figure 6.9: Continues data: Aged cell LLI:28% LAM_{PE}:18% LAM_{NE}:34%.

6.2.2 Down Sampled Data

Real-time data from the vehicle is collected in discrete time intervals. Therefore, validating the algorithm's accuracy with discrete time data is crucial. As discussed previously in the PyBaMM section, OCV points are typically collected after allowing the cell to relax. Thus, achieving better estimations from fewer data points will reduce computational costs. Fig. 6.10 shows the downsampled data.

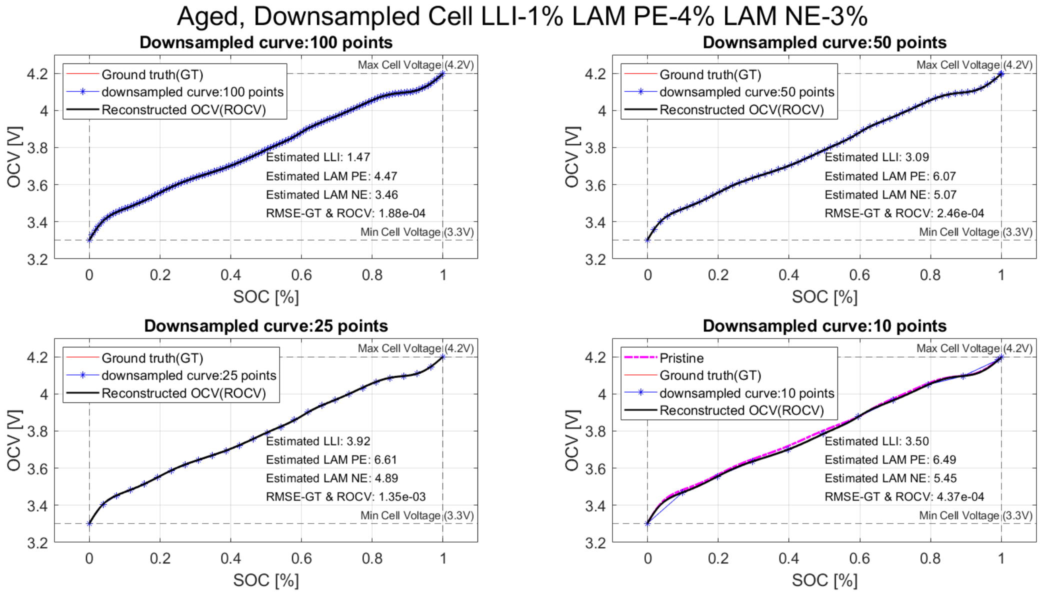

Figure 6.10: Down-sampled data: Aged cell LLI:1% LAM_{PE}:4% LAM_{NE}:3%.

In this experiment, continuous data were down-sampled to 100, 50, 25, and 10 points to check if the algorithm can accurately estimate degradation modes with fewer data points.

When down-sampled to 100 points, data were collected for every change in 1% SOC, resulting in 100 data points evenly distributed between 0% and 100% SOC. Similarly, for the other down-sampled points, data were collected at every 2%, 4%, and 10% SOC, respectively, for 50, 25, and 10 points. This approach was used to determine if the algorithm can still accurately estimate degradation modes with fewer data points.

In subplot 4, the down-sampled curve with 10 points includes pristine cell data to show how different degraded cell data looks compared to the pristine cell curve.

Fig 6.10 illustrates the down-sampled data points for an aged cell with degradation modes: LLI: 1%, LAM_{PE}: 40%, and LAM_{NE}: 3%. In the first subplot, 100 down-sampled points are used, and the estimated degradation modes are LLI: 1.47%, LAM_{PE}: 4.47%, and LAM_{NE}: 3.46%, showing an overall error of less than 0.5%. Results are similar for the other down-sampled points (see Table 6.2).

Table 6.2: Down sampled data comparison.

Down-sampled data: Aged cell LLI:1% LAM_{PE}:4% LAM_{NE}:3%.		
Down-sampled Points	Estimated Deg	RMSE
Continuous data	[1.00, 4.00, 3.00]	2.44×10^{-7}
100	[1.47, 4.47, 3.48]	5.88×10^{-4}
50	[3.09, 6.07, 5.07]	2.46×10^{-4}
25	[3.92, 6.61, 4.89]	1.35×10^{-3}
10	[3.50, 6.49, 5.45]	4.37×10^{-4}

The table demonstrates that as the number of sampled points decreases, the error in estimation increases compared to continuous data points. It can be seen that the estimation for 100 down-sampled points has the least amount of error compared to other down-sampled points and also has estimation values very close to the ground truth and continuous data, followed by down-sampled data of 50, 25, and 10 based on estimation accuracy. This can also be validated by looking at the RMSE value between the ground truth and reconstructed graph, where a similar trend is observed as shown in Table 6.2.

Table 6.3 contains data of different aged cells, down-sampled to 100, 50, 25, and 10 points as discussed previously. The previous inference showed that a higher number of sampling points, or in other words, more data points, results in better predictions. However, when the algorithm was tested with different aged cell data, it was observed that among the four down-sampled points, there are cases where 50 points give better estimations over 100 points and similar cases where 10 points give better estimations over 25 points. Despite these variations, the RMSE values between 100 and 50 points, or between 25 and 10 points, are not significantly different.

As mentioned in Subsection 7.2.1, due to non-convex nature of the problem there are instances where 50 points may perform better than 100 points. However, running the optimizer multiple times tends to result in 100 points outperforming the other three points. This demonstrates that while fewer points can occasionally yield better results, increasing the number of points generally leads to more reliable and accurate estimations.

Note: Table 6.3 data is arranged in terms of the least RMSE value first.

Table 6.3: Down sampled aged cells data comparison.

Down-sampled Points	Ground Truth	Estimated Deg	RMSE
100	[1,4,3]	[1.47, 4.47, 3.46]	1.88×10^{-4}
50		[3.09, 6.07, 5.07]	2.46×10^{-4}
10		[3.50, 6.49, 5.45]	4.37×10^{-4}
25		[3.92, 6.61, 4.89]	1.35×10^{-3}
50	[4,10,12]	[3.68, 9.71, 11.68]	2.49×10^{-4}
100		[3.43, 9.47, 11.46]	3.59×10^{-4}
25		[3.83, 9.83, 11.79]	6.57×10^{-4}
10		[3.70, 9.73, 11.67]	7.23×10^{-4}
100	[20,8,24]	[20.48, 8.57, 24.45]	1.06×10^{-3}
50		[19.9, 8.39, 24.59]	1.94×10^{-3}
25		[19.73, 8.20, 24.42]	2.00×10^{-3}
10		[18.83, 8.05, 24.86]	4.98×10^{-3}
50	[28,18,34]	[28.81, 19.37, 35.38]	1.82×10^{-3}
100		[26.92, 17.16, 33.61]	1.95×10^{-3}
10		[26.52, 17.12, 33.82]	3.85×10^{-3}
25		[26.88, 17.94, 34.80]	5.46×10^{-3}

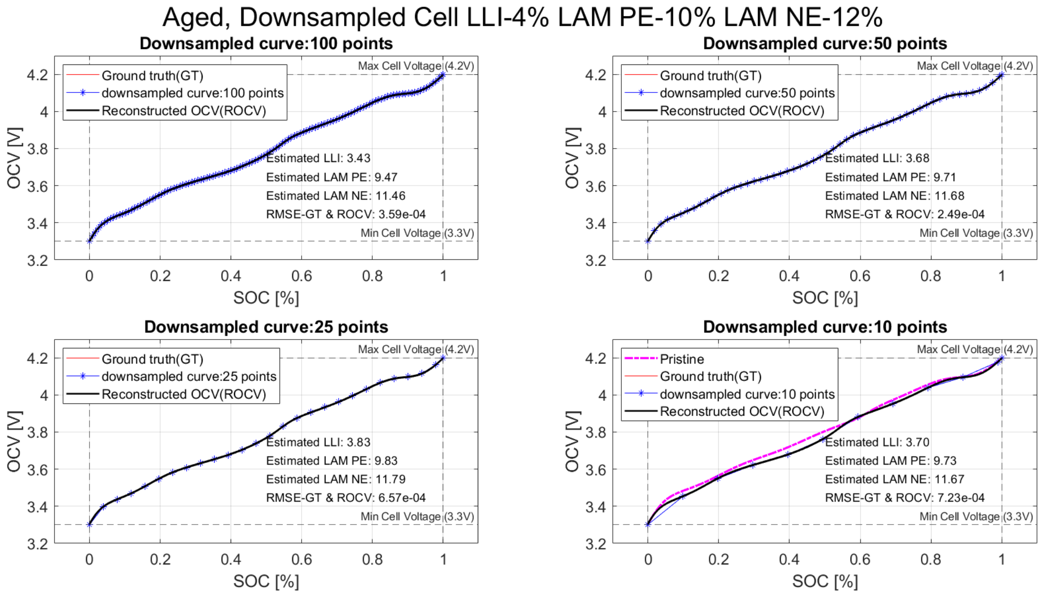

Figure 6.11: Down-sampled data: Aged cell LLI:4% LAM_{PE}:10% LAM_{NE}:12%.

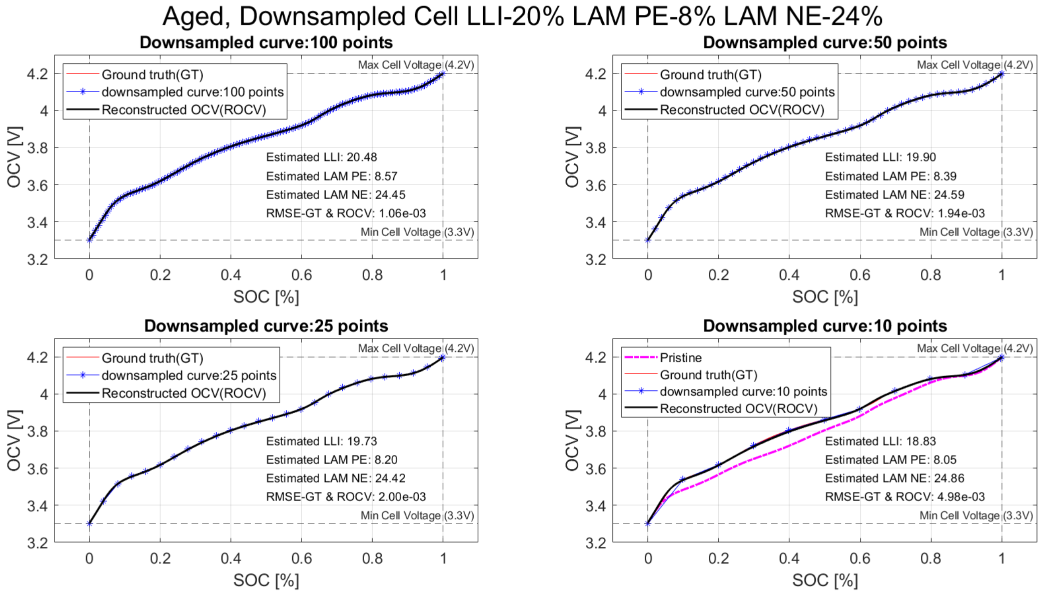

Figure 6.12: Down-sampled data: Aged cell LLI:20% LAM_{PE}:8% LAM_{NE}:24%.

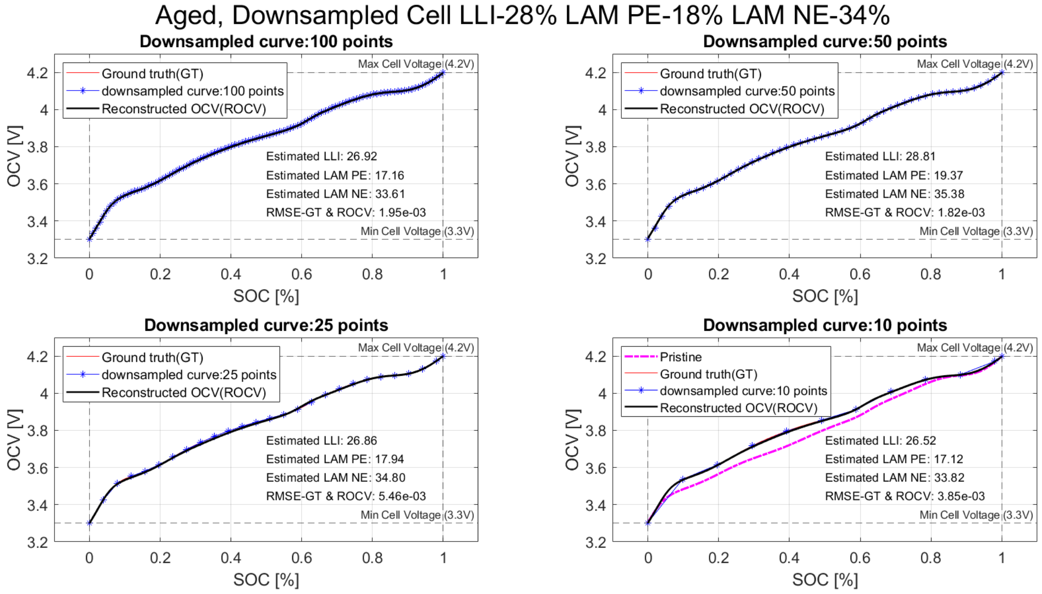

Figure 6.13: Down-sampled data: Aged cell LLI:28% LAM_{PE}:18% LAM_{NE}:34%.

In Fig. 6.10 to 6.13, data points from 100 to 25 down-sampled points provide enough points to fit a line between each point linearly, closely representing the ground truth. However, with only 10 down-sampled points (OCV voltage points for every 10% change in SOC), linearly interpolating between the points can lead to discrepancies between the down-sampled curve and the ground truth. This mismatch is particularly evident in the SOC regions from 0% to 10% and 90% to 100% SOC in Figures 6.10 to 6.13.

Despite these mismatches, the algorithm still provides estimations with error values between -1.5 and 3, and the reconstructed OCV curve closely follows the ground truth OCV. This indicates that even with just 10 sample points, updating the OCV curve is possible, which also aids in improving SOC estimation. This demonstrates the robustness of the algorithm in accurately estimating degradation modes and reconstructing OCV curves even with a minimal number of data points.

6.2.3 Down Sampled With Noise Data

Voltage sensor measurement data is commonly prone to noise, affecting the accuracy of estimations. In this test, we aim to evaluate the algorithm's performance when the data is subjected to white Gaussian noise. White Gaussian noise has noise power uniformly distributed over the entire frequency spectrum, and its amplitude follows a normal distribution with a mean of zero (indicating no bias) and a variance that determines the noise power. Higher variance indicates more powerful noise.

For this test, we chose five signal-to-noise ratio (SNR) values: 100, 60, 50, 45, and 40. SNR compares the level of the desired signal to the level of background noise:

- Higher SNR: Indicates that the signal is much stronger than the noise, leading to clearer and more accurate measurement data.
- Lower SNR: Indicates that the noise level is closer to the signal level, which can degrade the quality and accuracy of the signal.

An SNR value of 100 means the signal is purely the desired signal without noise. As the SNR value decreases, the amount of noise in the signal increases relative to the desired signal. This testing scenario helps understand how the algorithm performs under varying noise conditions and its robustness in providing accurate estimations despite the presence of noise.

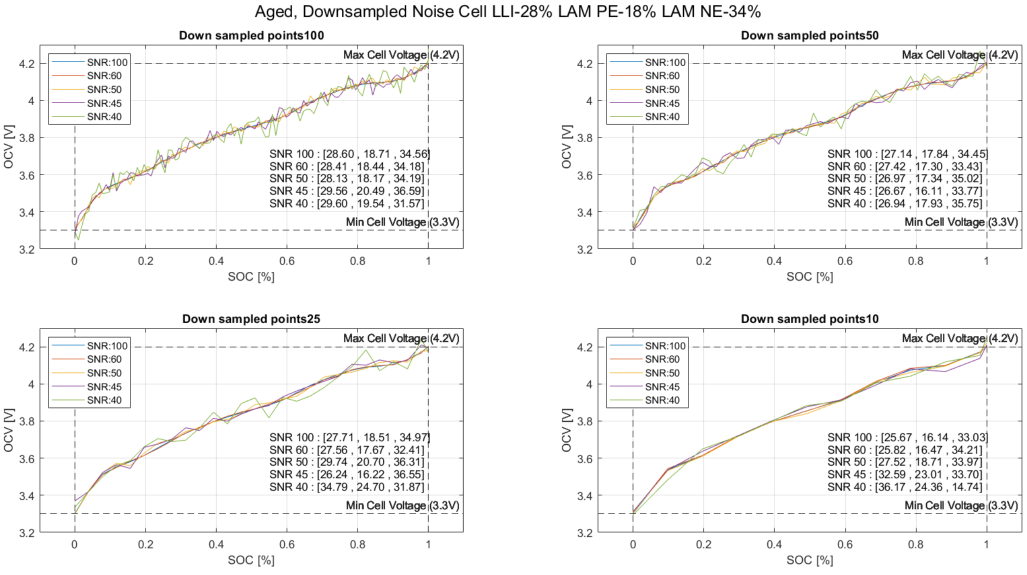

Figure 6.14: Down-sampled noise data: cell: LLI:28% LAM_{PE}:18% LAM_{NE}:34%.

Fig. 6.14 illustrates how noise affects the estimation of degraded cell sample data when combined with down-sampled data points. The results in this figure were generated by first down-sampling the continuous data points to 100, 50, 25, and 10, respectively. Then, white Gaussian noise was added to each down-sampled dataset with signal-to-noise ratio (SNR) values 100, 60, 50, 45, & 40. These datasets were provided as input to the algorithm.

In Fig. 6.14, there are four subplots, each representing one set of down-sampled points. Within each subplot, the input signal is visually depicted after adding noise to the down-sampled data. This visualization helps to understand how noise impacts the quality of the input data at different SNR levels and down-sampling resolutions.

Table 6.4: Down sampled noise data.

Down-sampled noise data: cell: LLI:28% LAM_{PE}:18% LAM_{NE}:34%.		
Down-sampled Points	SNR	Estimated Deg
100	100	[28.60, 18.71, 34.56]
	60	[28.41, 18.44, 34.18]
	50	[28.13, 18.17, 34.19]
	45	[29.56, 20.49, 36.59]
	40	[29.60, 19.54, 31.57]
25	100	[27.71, 18.51, 34.97]
	60	[27.56, 17.67, 32.41]
	50	[29.74, 20.70, 36.41]
	45	[26.24, 16.22, 36.55]
	40	[34.79, 24.70, 31.87]

Table 6.4 presents the estimation data for degraded cell data depicted in Fig. 6.14. To simplify and avoid cluttering the table with excessive data points, only two down-sampled datasets are considered: 100 and 25 down-sampled points.

From the table, it is evident that as the SNR value decreases, the error in estimation increases. For instance, considering the cell data for 100 down-sampled points mentioned in Table 6.4 and Fig. 6.14, with an SNR of 100, the algorithm estimates degradation modes as LLI: 28.60%, LAM_{PE}: 18.71%, and LAM_{NE}: 34.56%, close to the ground truth values of LLI: 28%, LAM_{PE}: 18%, and LAM_{NE}: 34%. However, under the worst-case scenario with an SNR of 40, the error in estimation increases, and the algorithm estimates degradation modes as LLI: 29.60%, LAM_{PE}: 19.54%, and LAM_{NE}: 31.57%.

Similarly, for the case of 25 down-sampled points, the error in estimation also increases as the SNR decreases. When comparing the estimation generated using 100 and 25 down-sampled points, it's evident that 100 down-sampled points provide a better estimation. For instance, with an SNR of 40, the estimates for 100 down-sampled points are closer to the ground truth compared to those for 25 down-sampled points. This indicates that having more measured voltage data points, even with higher noise levels, still provides a very good estimation.

To avoid the clustering the plot with graphs only 100 and 25 down sampled points with SNR value 60, 50 & 45 are presented from here on (see Fig. 6.15 to 6.18).

The figures show the degradation modes estimation and reconstruction of the OCV curve data for different degraded cells. In these figures, the first subplot consists of three curves representing data down-sampled to 100 points with SNR values of 60, 50, and 45, respectively. Additionally, the pristine cell OCV curve is included to show how the degraded cell OCV curves compare to the pristine cell curve. These three noise-affected signals are input into the algorithm to estimate degradation modes, which are shown in subplot 1 and also summarized in Table 6.5 and 6.6.

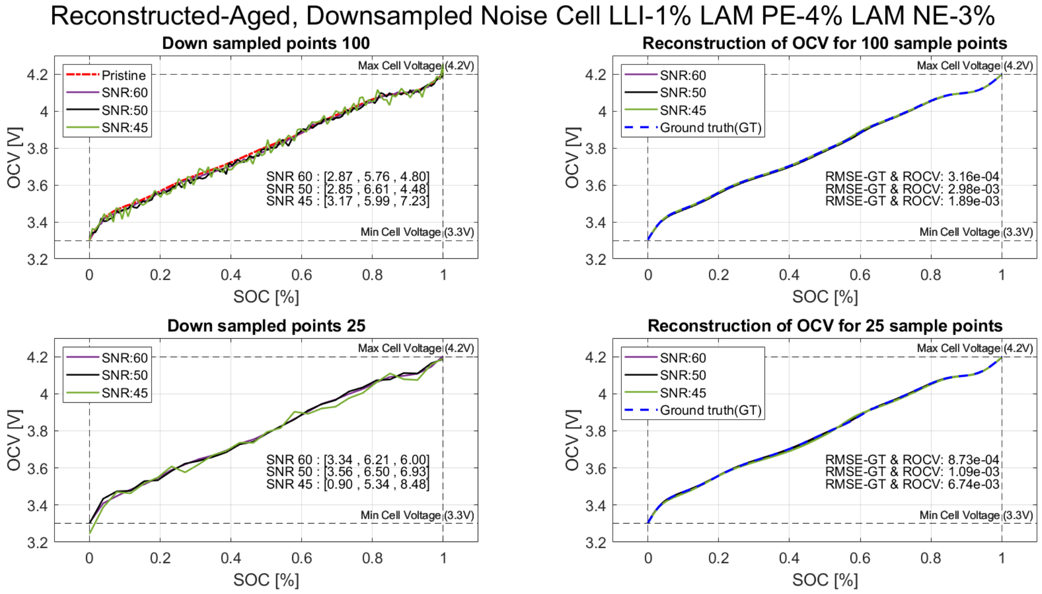

Figure 6.15: Reconstructed Down-sampled noise data: cell: LLI:1% LAM_{PE}:4% LAM_{NE}:3%.

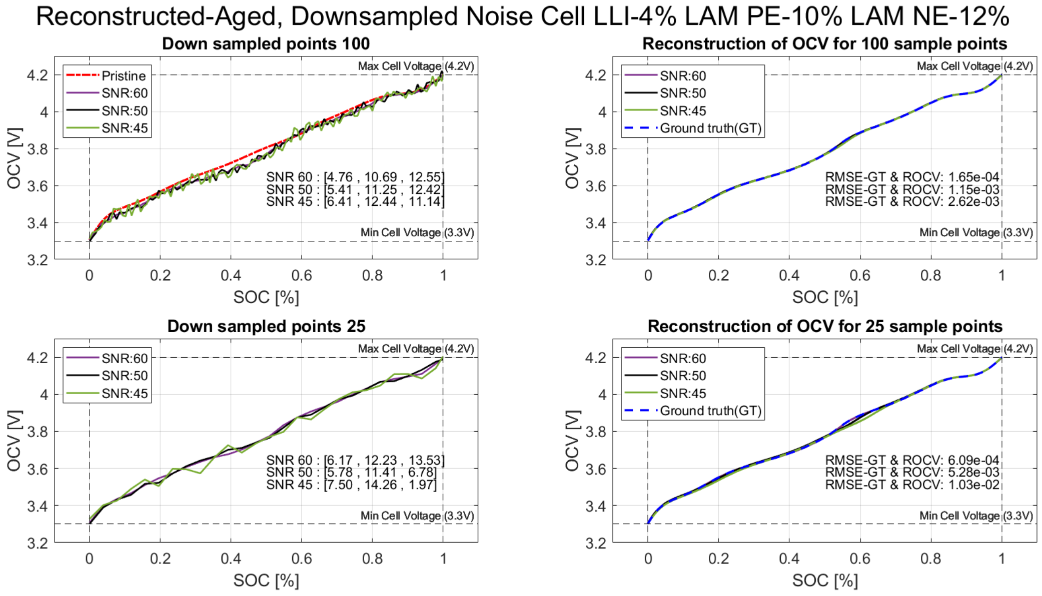

Figure 6.16: Reconstructed Down-sampled noise data: cell: LLI:4% LAM_{PE}:10% LAM_{NE}:12%.

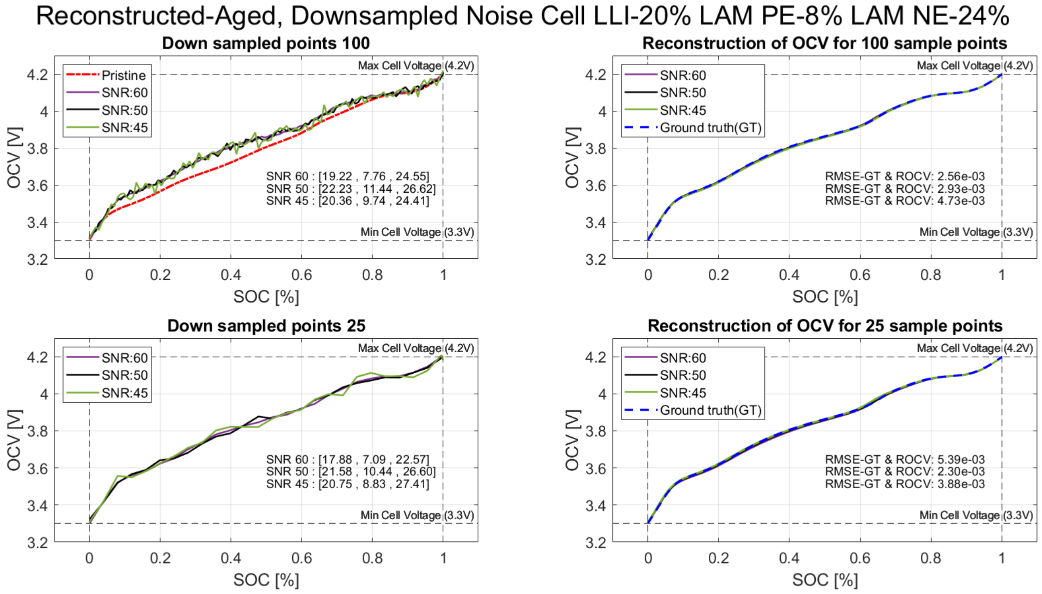

Figure 6.17: Reconstructed Down-sampled noise data: cell: LLI:20% LAM_{PE}:8% LAM_{NE}:24%.

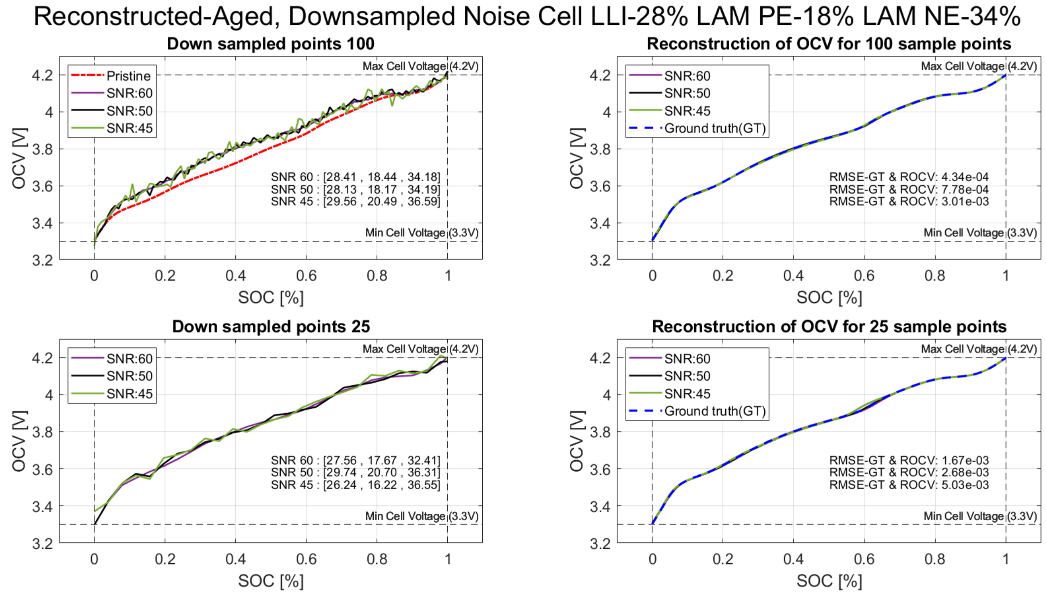

Figure 6.18: Reconstructed Down-sampled noise data: cell: LLI:28% LAM_{PE}:18% LAM_{NE}:34%.

The estimated degradation modes are then used to reconstruct the OCV curve, as shown in subplot 2 of each figure. In this subplot, the RMSE between the ground truth and reconstructed curve is calculated and shown in both the plot and Table 6.5 and 6.6. A similar procedure was followed for the down-sampled points (25 points), with data presented in subplots 3 and 4, respectively.

Table 6.5: Down sampled points:noise data comparison.

Down sampled points: 100.			
SNR	Ground Truth	Estimated Deg	RMSE
60	[1,4,3]	[2.87, 5.76, 4.80]	3.16×10^{-4}
50		[2.85, 6.61, 4.48]	2.98×10^{-3}
45		[3.17, 5.99, 7.23]	1.89×10^{-3}
60	[4,10,12]	[4.76, 10.69, 12.55]	1.65×10^{-4}
50		[5.41, 11.25, 12.42]	1.15×10^{-3}
45		[6.41, 12.44, 11.14]	2.62×10^{-3}
60	[20,8,24]	[19.22, 7.76, 24.55]	2.56×10^{-3}
50		[22.23, 11.44, 26.62]	2.93×10^{-3}
45		[20.36, 9.74, 24.41]	4.73×10^{-3}
60	[28,18,34]	[28.41, 18.44, 34.18]	4.34×10^{-4}
50		[28.13, 18.17, 34.19]	7.78×10^{-4}
45		[29.56, 20.49, 36.59]	3.01×10^{-3}

Inferring from Table 6.5 and Fig. 6.15 to 6.18, it can be clearly seen that as the SNR value decreases, the error in the estimation increases, and the discrepancy between the ground truth and reconstructed curve grows, thus increasing the RMSE value. Considering the case where the ground truth values are LLI: 4%, LAM_{PE}: 10%, and LAM_{NE}: 12%, as shown in Table 6.5, the lowest RMSE value is 1.6×10^{-4} for SNR: 60. The next lowest RMSE value is 1.15×10^{-3} for SNR: 50, and the highest RMSE value is 2.62×10^{-3} for SNR: 45. A similar pattern is observed with the down-sampled data of 25 points, as shown in Table 6.6.

In the down-sampled data of 100 points for the ground truth values LLI: 1%, LAM_{PE}: 4%, and LAM_{NE}: 3%, as shown in Table 6.5, a slightly different trend is observed. Specifically, the case with SNR 45 has a slightly lower RMSE error and better estimation than the SNR 50. This occurs due to the non-convexity of the problem, meaning multiple solutions exist. Additionally, the outcome depends on the initial point of search in the optimization process. This issue can be mitigated by running the global search optimization multiple times and averaging the estimations.

Table 6.6: Down sampled noise data comparison.

Down sampled points: 25.			
SNR	Ground Truth	Estimated Deg	RMSE
60 50 45	[1,4,3]	[3.34, 6.21, 6.00] [3.56, 6.50, 6.93] [0.90, 5.34, 8.48]	8.73×10^{-4} 1.09×10^{-3} 6.74×10^{-3}
60 50 45	[4,10,12]	[6.17, 12.23, 13.53] [5.78, 11.41, 6.78] [7.50, 14.26, 1.97]	6.09×10^{-4} 5.28×10^{-3} 1.03×10^{-2}
60 50 45	[20,8,24]	[17.88, 7.09, 22.57] [21.58, 10.44, 26.60] [20.75, 8.83, 27.41]	5.39×10^{-3} 2.30×10^{-3} 3.88×10^{-3}
60 50 45	[28,18,34]	[27.56, 17.67, 32.41] [29.74, 20.70, 36.31] [26.24, 16.22, 36.55]	1.67×10^{-3} 2.68×10^{-3} 5.03×10^{-3}

Table 6.7 showcases comprehensive data about the RMSE values for a degraded cell with LLI: 28%, LAM_{PE}: 18%, and LAM_{NE}: 40%, by varying the down-sampling data and SNR values. This table illustrates how these two factors interplay to influence the accuracy of OCV reconstruction.

When examining the RMSE across different configurations, a consistent trend emerges: with a high number of down-sampled points, such as 100, the RMSE values remain relatively low across all SNR levels. This indicates that with more data points, the OCV can be reconstructed with higher accuracy even in noisier conditions. Conversely, as the number of down-sampled points decreases to 50, 25, and then 10, the RMSE values rise notably for each SNR level. This increase is more pronounced at lower SNR values. For instance, with only 10 down-sampled points, the RMSE escalates from 4.67×10^{-3} at SNR:60 to 2.08×10^{-2} at SNR:40. This dramatic rise suggests that fewer data points make the signal reconstruction highly susceptible to noise, resulting in greater errors.

Thus, the combined effect shows that high accuracy is maintained only when both the number of down-sampled points is high and the SNR is high. On the other hand, a reduction in either parameter, and more so in both, leads to a substantial increase in RMSE, highlighting the importance of maintaining both adequate data points and low noise in the measurement process.

Table 6.7: Down sampled points and corresponding SNR values

Down-sampled noise data: cell: LLI:28% LAM_{PE}:18% LAM_{NE}:34%.				
Down sampled	SNR:60	SNR:50	SNR:45	SNR:40
100	4.34×10^{-4}	7.78×10^{-4}	3.01×10^{-3}	4.67×10^{-3}
50	9.09×10^{-4}	3.09×10^{-3}	2.45×10^{-3}	5.21×10^{-3}
25	1.67×10^{-3}	2.68×10^{-3}	5.03×10^{-3}	9.98×10^{-3}
10	4.67×10^{-3}	4.99×10^{-3}	6.10×10^{-3}	2.08×10^{-2}

6.2.4 Segmented Data

The statistics show that in day-to-day usage, customers rarely fully discharge their batteries. Consequently, collecting the OCV curve across the entire SOC range is challenging. Based on the statistics, the average customer tends to discharge the battery to around 60% or higher and charges it back by the end of the day. Therefore, only segments of the OCV curve can be acquired. Verifying if the algorithm can still accurately estimate the degradation modes given a segment of data would help in implementing this algorithm on real-time hardware.

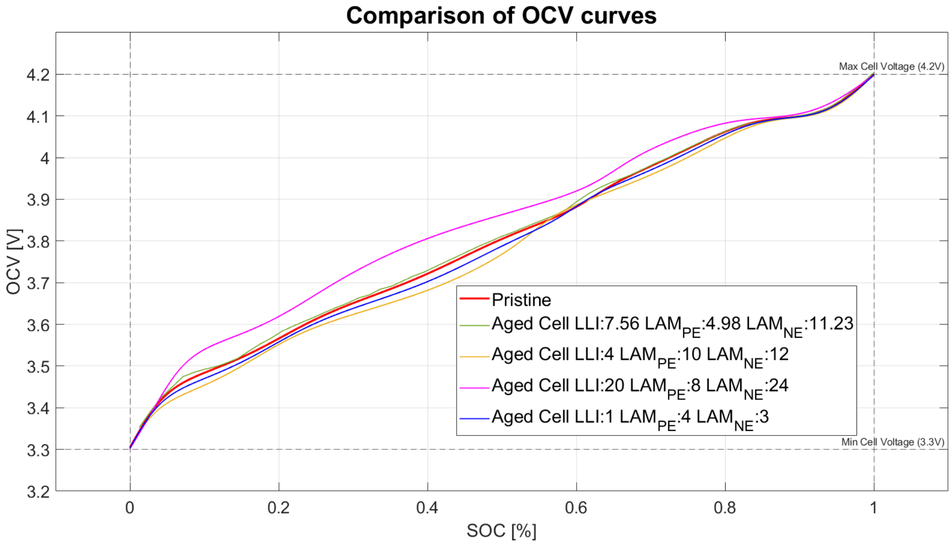

Figure 6.19: OCV curve comparison for segmentation.

Fig. 6.19 illustrates the OCV curves of different aged cells alongside the pristine curve. To determine which segment of the data should be fed into the algorithm for accurately estimating degradation modes and reconstructing the OCV curve, it is crucial to choose the segmentation start and end points wisely. Estimating degradation modes relies on changes in the OCV, which indirectly affect the shifting and scaling of the OCP curves. Therefore, it is important to select regions that clearly distinguish one degraded cell from another, given the non-convex nature of the problem.

From Fig. 6.19, it is evident that the SOC range from 0.8 to 0.4 allows the curves to be clearly distinguished compared to other segments. This segment of information can therefore be used to estimate degradation modes and reconstruct the OCV curve with greater accuracy.

In contrast, the SOC range from 0.8 to 1 shows significant overlap among all the curves, which could make it challenging for the algorithm to estimate the degradation modes accurately. Based on these observations from Fig. 6.19, tests have been conducted on different degraded cells to verify if segmented data can accurately estimate degradation modes.

In these tests, the continuous data set was first selected, and then the required segmented data was cropped and input into the algorithm, which estimated the degradation modes. The OCV curve reconstruction was done based on these estimations. To further validate the algorithm, tests were also conducted by down-sampling the continuous data and adding noise. Based on previous inferences from the subsection "Down Sampled With Noise Data," maintaining both adequate data points and low noise in the measurement process yields better estimations. Therefore, down-sampled points: 100 was chosen. This means in the 0.4 to 0.8 SOC segment, there will be 40 data points. Reducing the down-sampled points might not provide sufficient information about the curve, and an SNR value of 50 was chosen for these tests.

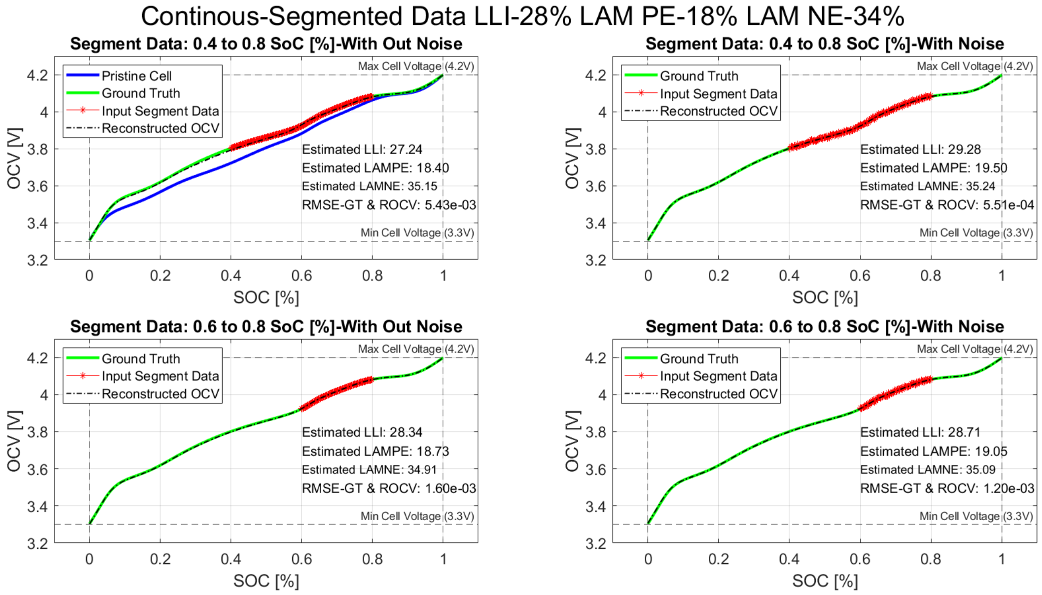

Figure 6.20: Segmented 0.8 to 1, continuous data, aged cell data LLI: 28 LAM_{PE}: 18 LAM_{NE}: 34.

Fig. 6.20 illustrates the test results of a segmented OCV curve for a cell aged to LLI: 28%, LAM_{PE}: 18%, and LAM_{NE}: 34%. In the first subplot, the OCV curve segment from 0.4 to 0.8 SOC is represented by red stars and given as input. The estimated degradation modes are LLI: 27.24%, LAM_{PE}: 18.40%, and LAM_{PE}: 35.15%, with the reconstructed OCV curve showing an RMSE of 5.43×10^{-3}.

To the same segmented data is then added noise at SNR: 50. The estimated degradation modes in this noisy scenario are LLI: 29.28%, LAM_{PE}: 19.50%, and LAM_{NE}: 35.09%, with the reconstructed OCV curve showing an RMSE of 5.51×10^{-4}. By comparing both the noisy and non-noisy situations, it is evident that the segment without noise has slightly better estimations, as indicated by the lower RMSE value, which means that the OCV reconstruction is slightly more accurate without noise.

A similar procedure is followed for the segment from 0.6% to 0.8% SOC, as shown in the bottom subplot of Fig. 6.20. The previous continuous cell data is down-sampled to 100 points, and similar segmentation is performed and shown in Fig. 6.21.

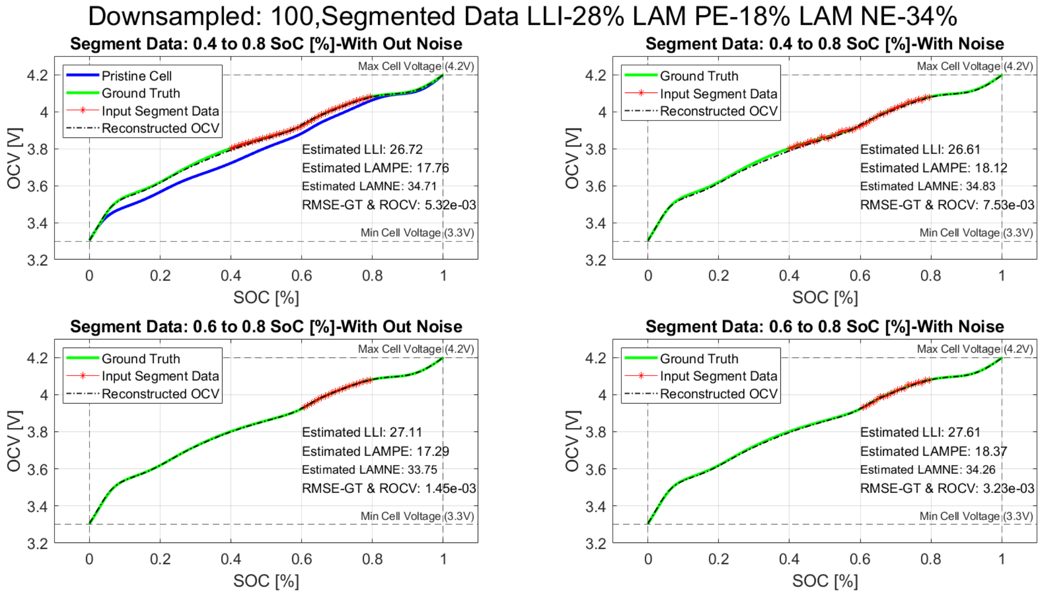

Figure 6.21: Segmented 0.4 to 0.6, downsampled:100, aged cell data LLI: 28 LAM_{PE}: 18 LAM_{NE}: 34.

The analysis of segmented OCV data without noise, as shown in Table 6.8, highlights several important trends. The SOC segment from 0.6 to 0.8 consistently demonstrates the lowest RMSE values, indicating it is more accurately estimating degradation modes. Conversely, the 0.9 to 1 segment shows the highest RMSE, reflecting difficulties in estimation due to significant curve overlap. When comparing continuous data to down-sampled data (100 points), it is evident that down-sampling generally maintains or even slightly improves accuracy in some segments. The data suggests that higher accuracy is achieved in segments with minimal curve overlap and adequate data points, while segments with overlapping OCV curves (e.g., 0.9 to 1) result in higher errors. Therefore, selecting well-defined SOC segments is crucial for accurate degradation mode estimation, and down-sampling to 100 points can be effective in maintaining high accuracy.

Table 6.8: Without noise segmented data comparison.

Cell data without noise: LLI:28% LAM_{PE}:18% LAM_{NE}:34%.			
Down sample	SOC Segment	Estimated Deg	RMSE
Continuous	0.4% to 0.8%	[27.24, 18.40, 35.15]	5.43×10^{-3}
Continuous	0.6% to 0.8%	[28.24, 18.73, 34.91]	1.60×10^{-3}
Continuous	0.8% to 1%	[25.46, 15.43, 31.96]	2.2×10^{-3}
Continuous	0.9% to 1%	[25.10, 15.87, 26.10]	9.19×10^{-3}
100	0.4% to 0.8%	[26.72, 17.76, 34.71]	5.32×10^{-3}
100	0.6% to 0.8%	[27.11, 17.29, 33.75]	1.45×10^{-3}
100	0.8% to 1%	[30.09, 20.65, 36.22]	1.22×10^{-3}
100	0.9% to 1%	[29.52, 21.18, 31.94]	8.43×10^{-3}

The analysis of segmented OCV data with noise, as presented in Table 6.9, reveals several key trends. The SOC segment from 0.4 to 0.8 consistently demonstrates the lowest RMSE values for both continuous and down-sampled data, indicating this range is most effective for accurately estimating degradation modes, even in the presence of noise. Conversely, the segments from 0.8 to 1 and 0.9 to 1 show significantly higher RMSE values, reflecting the challenges in estimation due to overlapping OCV curves and the impact of noise. Notably, the RMSE values for the 100 down-sampled points are generally higher than those for continuous data. These data has been illustrated in the Fig. 6.20 to 6.23.

Table 6.9: With noise segmented data comparison.

Cell data with noise: LLI:28% LAM_{PE}:18% LAM_{NE}:34%.			
Down sample	SOC Segment	Estimated Deg	RMSE
Continuous	0.4% to 0.8%	[29.28, 19.50, 35.24]	5.51×10^{-4}
Continuous	0.6% to 0.8%	[28.71, 19.05, 35.09]	1.20×10^{-3}
Continuous	0.8% to 1%	[28.66, 23.13, 25.61]	2.46×10^{-2}
Continuous	0.9% to 1%	[28.05, 21.70, 29.06]	1.85×10^{-2}
100	0.4% to 0.8%	[26.61, 18.12, 34.83]	7.53×10^{-3}
100	0.6% to 0.8%	[27.61, 18.37, 34.26]	3.23×10^{-3}
100	0.8% to 1%	[30.81, 15.90, 36.77]	2.34×10^{-2}
100	0.9% to 1%	[31.65,19.92, 31.6]	9.98×10^{-3}

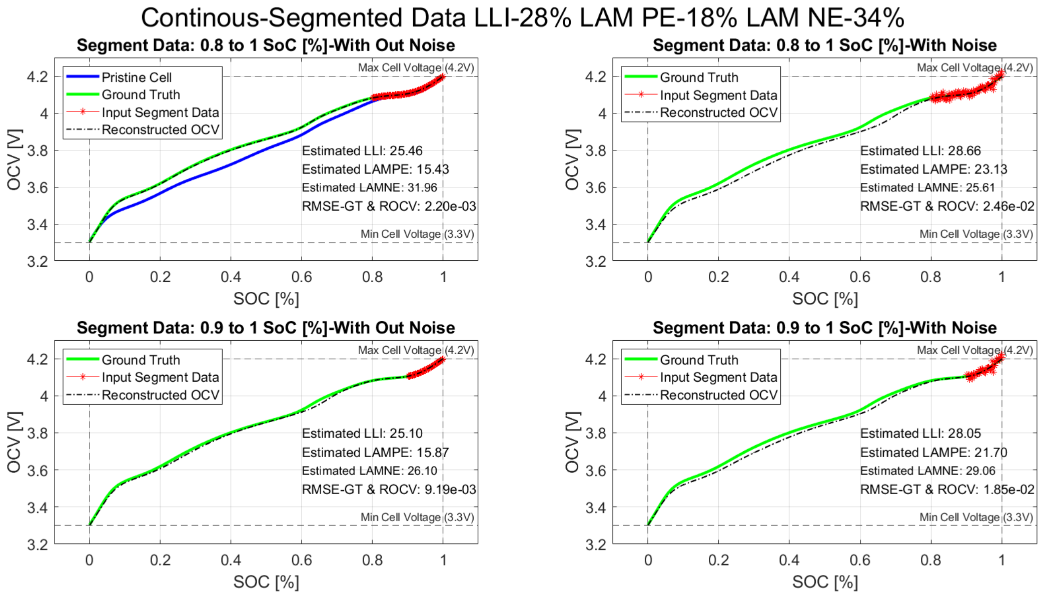

Figure 6.22: Segmented 0.8 to 1, continuous data, aged cell data LLI: 28 LAM_{PE}: 18 LAM_{NE}: 34.

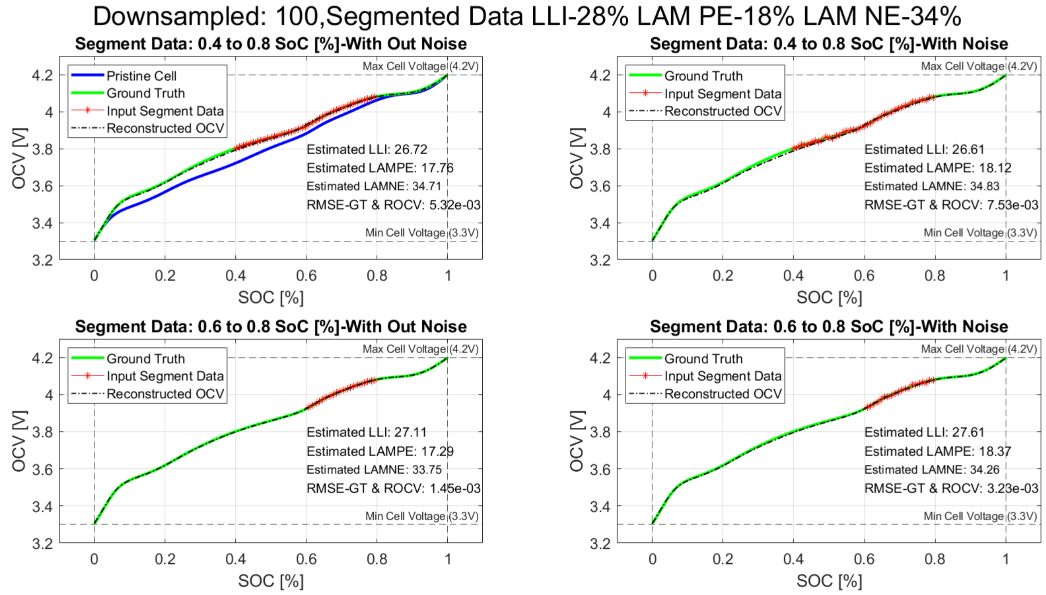

Figure 6.23: Segmented 0.4 to 0.8, downsampled:100, aged cell data LLI: 28 LAM_{PE}: 18 LAM_{NE}: 34.

By examining both Table 6.8 and Table 6.9, clear trends emerge regarding the estimation of degradation modes from segmented OCV data, both with and without noise. In the absence of noise, the SOC segments from 0.4 to 0.8 and 0.6 to 0.8 consistently show low RMSE values, indicating these segments provide the most accurate degradation mode estimations. The segment from 0.8 to 1 shows a higher RMSE, reflecting less accurate estimations due to overlapping curves in this range.

When noise is introduced, the SOC segment from 0.4 to 0.8 remains the most reliable for both continuous and down-sampled data, maintaining relatively low RMSE values. However, the RMSE values increase more noticeably for the segments from 0.8 to 1 and 0.9 to 1, indicating that noise worsen the estimation in these ranges. The down-sampled data at 100 points generally exhibits higher RMSE values compared to continuous data, further highlighting the susceptibility to noise.

Overall, the SOC segments from 0.4 to 0.8 and 0.6 to 0.8 are most effective for accurate degradation mode estimation, even under noisy conditions. This underscores the importance of choosing segments with distinct curve features and maintaining a high number of data points to minimize the impact of noise on the estimation accuracy.

7

Conclusion

This thesis has presented a novel approach for estimating degradation modes in lithium-ion batteries, leveraging advanced algorithmic techniques to enhance the accuracy and reliability of degradation diagnosis. The research addresses the critical need for efficient and precise monitoring of battery health, which is paramount in applications ranging from consumer electronics to electric vehicles and large-scale energy storage systems.

This study resulted in a successfully developed and validated algorithm capable of identifying and estimating various degradation modes in lithium-ion batteries. This robust algorithm integrates data-driven models with battery operational data, facilitating a comprehensive understanding of degradation mechanisms.

Validating the algorithm through experiments, encompassed various scenarios, including continuous, down-sampled, and noise-affected data, ensuring a robust evaluation of the algorithm's performance. Continuous data results confirmed the algorithm's ability to track OCV curves accurately, despite the non-convex nature of the problem, which introduces challenges due to multiple local minima. Through optimization constraints and multiple runs, the reliability of the estimations was improved.

The performance with down-sampled data revealed that while reducing the number of data points increases estimation error, the algorithm still provides reasonably accurate results. For instance, 100 down-sampled points resulted in minimal error, making it a viable approach for practical applications. Even with as few as 10 points, the algorithm maintained a close alignment with the ground truth degradation modes, demonstrating its robustness. When noise was introduced, the algorithm's performance naturally degraded as SNR values decreased. However, the estimations remained within acceptable error margins, indicating the algorithm's resilience in noisy environments. Higher SNR values, particularly above 50, yielded better accuracy, underscoring the importance of maintaining good signal quality.

Segmented data analysis further validated the algorithm's efficacy in real-world conditions where complete OCV curves might not always be available. Selecting appropriate SOC segments, particularly from 40% to 80%, proved crucial for accurate estimations. Even under noisy and down-sampled conditions, the algorithm effectively estimated the degradation modes fairly accurately; reconstructed OCV curves were in comparable accuracy to continuous data.

8

Future Works

Building on the advancements presented in this thesis, several promising directions for future research have been identified. These avenues aim to enhance the robustness, applicability, and accuracy of the developed algorithm for estimating degradation modes in lithium-ion batteries.

8.1 Battery Capacity relation

Investigating the direct relationship between various degradation modes and battery capacity could help refine the model. By understanding how different degradation mechanisms impact overall battery capacity, it may be possible to develop more individualized constraint, thereby reducing sensitivity to local minima.

8.2 Cell to Pack/Module level scaling

The current algorithm is designed for individual cell-level analysis. Extending this to battery pack or module levels involves significant complexity due to the interactions between multiple cells. Future research should focus on adapting the algorithm to handle these larger systems effectively. With limited sensors available, it is crucial to develop methods to pinpoint degradation at the module or pack level accurately.

8.3 Cell Chemistries

To ensure the generalization of the algorithm, it is essential to test its performance with various battery chemistries, such as LFP and LCO. Different chemistries exhibit unique degradation patterns, and the algorithm must be validated and possibly adapted to handle these variations effectively.

8.4 Noise in SOC calculation

The current implementation primarily considers errors in voltage measurements. Future work should include scenarios where SOC estimations are erroneous. Developing methods to correct or compensate for SOC estimation errors can be crucial to enhance the overall accuracy and reliability of the degradation estimation process.

8.5 Feasibility

Future work should also explore the feasibility of embedding these advanced algorithms within BMS for real-time health monitoring and prediction. This includes developing lightweight, computationally efficient versions of the algorithm suitable for real-time applications.

In summary, while this research has laid a foundation for estimating degradation modes in lithium-ion batteries, the proposed future work aims to expand its capabilities and applications. Addressing these areas will contribute to the development of more reliable, efficient, and sustainable battery systems, meeting the growing demands of modern technology and energy solutions.

Bibliography

[1] F Brosa Planella, W Ai, A M Boyce, A Ghosh, I Korotkin, S Sahu, V Sulzer, R Timms, T G Tranter, M Zyskin, S J Cooper, J S Edge, J M Foster, M Marinescu, B Wu, and G Richardson. “A continuum of physics-based lithium-ion battery models reviewed”. In: *Progress in Energy* 4.4 (July 2022), p. 042003. DOI: `10.1088/2516-1083/ac7d31`.

[2] Simon E. J. O’Kane, Weilong Ai, Ganesh Madabattula, Diego Alonso-Alvarez, Robert Timms, Valentin Sulzer, Jacqueline Sophie Edge, Billy Wu, Gregory J. Offer, and Monica Marinescu. “Lithium-ion battery degradation: how to model it”. In: *Phys. Chem. Chem. Phys.* 24 (13 2022), pp. 7909–7922. DOI: `10.1039/D2CP00417H`.

[3] Jacqueline S. Edge, Simon O’Kane, Ryan Prosser, Niall D. Kirkaldy, Anisha N. Patel, Alastair Hales, Abir Ghosh, Weilong Ai, Jingyi Chen, Jiang Yang, Shen Li, Mei-Chin Pang, Laura Bravo Diaz, Anna Tomaszewska, M. Waseem Marzook, Karthik N. Radhakrishnan, Huizhi Wang, Yatish Patel, Billy Wu, and Gregory J. Offer. “Lithium ion battery degradation: what you need to know”. In: *Phys. Chem. Chem. Phys.* 23 (14 2021), pp. 8200–8221. DOI: `10.1039/D1CP00359C`.

[4] Chang-Hui Chen, Ferran Brosa Planella, Kieran O’Regan, Dominika Gastol, W. Dhammika Widanage, and Emma Kendrick. “Development of Experimental Techniques for Parameterization of Multi-scale Lithium-ion Battery Models”. In: *Journal of The Electrochemical Society* 167.8 (May 2020), p. 080534. DOI: `10.1149/1945-7111/ab9050`.

[5] Giulia Carbonaro. *Electric vehicles: EU approves new law to add more chargers across Europe.* May 2023.

[6] Ping Liu, John Wang, Jocelyn Hicks-Garner, Elena Sherman, Souren Soukiazian, Mark Verbrugge, Harshad Tataria, James Musser, and Peter Finamore. “Aging Mechanisms of LiFePO4 Batteries Deduced by Electrochemical and Structural Analyses”. In: *Journal of The Electrochemical Society - J ELECTROCHEM SOC* 157 (Jan. 2010). DOI: `10.1149/1.3294790`.

[7] Christoph R. Birkl, Matthew R. Roberts, Euan McTurk, Peter G. Bruce, and David A. Howey. “Degradation diagnostics for lithium ion cells”. In: *Journal of Power Sources* 341 (2017), pp. 373–386. ISSN: 0378-7753. DOI: `https://doi.org/10.1016/j.jpowsour.2016.12.011`.

[8] *PRODUCT SPECIFICATION; Rechargeable Lithium Ion Battery; Model : INR21700 M50 18.20Wh.* LRB-PS-CY18.2Wh-M50. Rev. 0. LG Chem. Aug. 2016.

[9] *LG 21700 M50 5000mAh (Grey).* Rev. 1.0. lygte-info. Mar. 2012.

[10] Cheng Lin, Aihua Tang, Hao Mu, Wenwei Wang, and Chun Wang. "Aging Mechanisms of Electrode Materials in Lithium-Ion Batteries for Electric Vehicles". In: *Journal of Chemistry* 2015 (June 2015). DOI: `10.1155/2015/104673`.

[11] Jorn Reniers, Grietus Mulder, and David Howey. "Review and Performance Comparison of Mechanical-Chemical Degradation Models for Lithium-Ion Batteries". In: *Journal of The Electrochemical Society* 166 (Sept. 2019), A3189–A3200. DOI: `10.1149/2.0281914jes`.

[12] Stephen J. Harris, David J. Harris, and Chen Li. "Failure statistics for commercial lithium ion batteries: A study of 24 pouch cells". In: *Journal of Power Sources* 342 (2017), pp. 589–597. ISSN: 0378-7753. DOI: `https://doi.org/10.1016/j.jpowsour.2016.12.083`.

[13] Matthieu Dubarry, Nan Qin, and Paul Brooker. "Calendar Aging of commercial Li-ion cells of different chemistries – A review". In: *Current Opinion in Electrochemistry* 9 (June 2018). DOI: `10.1016/j.coelec.2018.05.023`.

[14] Alexander Karger, Julius Schmitt, Cedric Kirst, Jan Singer, Leo Wildfeuer, and Andreas Jossen. "Mechanistic calendar aging model for lithium-ion batteries". In: *Journal of Power Sources* Volume 578 (Sept. 2023), p. 233208. DOI: `10.1016/j.jpowsour.2023.233208`.

[15] Kevin Gering, Sergiy Sazhin, David Jamison, Christopher Michelbacher, Bor Yann Liaw, Matthieu Dubarry, and Mikaël Cugnet. "Investigation of path dependence in commercial lithium-ion cells chosen for plug-in hybrid vehicle duty cycle protocols". In: *Journal of Power Sources* 196 (Apr. 2011), pp. 3395–3403. DOI: `10.1016/j.jpowsour.2010.05.058`.

[16] Jeremy P. Meyers, Marc Doyle, Robert M. Darling, and John Newman. "The Impedance Response of a Porous Electrode Composed of Intercalation Particles". In: *Journal of The Electrochemical Society* 147.8 (Aug. 2000), p. 2930. DOI: `10.1149/1.1393627`.

[17] Matthieu Dubarry, Cyril Truchot, and Bor Yann Liaw. "Synthesize battery degradation modes via a diagnostic and prognostic model". In: *Journal of Power Sources* 219 (2012), pp. 204–216. ISSN: 0378-7753. DOI: `https://doi.org/10.1016/j.jpowsour.2012.07.016`.

[18] Julius Schmitt, Markus Schindler, Andreas Oberbauer, and Andreas Jossen. "Determination of degradation modes of lithium-ion batteries considering aging-induced changes in the half-cell open-circuit potential curve of silicon–graphite". In: *Journal of Power Sources* 532 (2022), p. 231296. ISSN: 0378-7753. DOI: `https://doi.org/10.1016/j.jpowsour.2022.231296`.

[19] Alexander Karger, Julius Schmitt, Cedric Kirst, Jan Singer, Leo Wildfeuer, and Andreas Jossen. "Mechanistic calendar aging model for lithium-ion batteries". In: *Journal of Power Sources* Volume 578 (Sept. 2023), p. 233208. DOI: `10.1016/j.jpowsour.2023.233208`.

[20] Chen Zhu, Liqing Sun, Cheng Chen, Jinpeng Tian, Weixiang Shen, and Rui Xiong. "Lithium-ion battery degradation diagnosis and state-of-health estimation with half cell electrode potential". In: *Electrochimica Acta* 459 (2023), p. 142588. ISSN: 0013-4686. DOI: `https://doi.org/10.1016/j.electacta.2023.142588`.

[21] Niall Kirkaldy, Mohammad A. Samieian, Gregory J. Offer, Monica Marinescu, and Yatish Patel. "Lithium-ion battery degradation: Comprehensive cycle ageing data and analysis for commercial 21700 cells". In: *Journal of Power Sources* 603 (2024), p. 234185. ISSN: 0378-7753. DOI: `https://doi.org/10.1016/j.jpowsour.2024.234185`.

[22] Pietro Iurilli, Claudio Brivio, Rafael Carrillo, and Vanessa Wood. "Physics-Based SoH Estimation for Li-Ion Cells". In: *Batteries* 8 (Nov. 2022), p. 204. DOI: `10.3390/batteries8110204`.

[23] Ming-Ying Zhou, Jian-Bang Zhang, Chi-Jyun Ko, and Kuo-Ching Chen. "Precise prediction of open circuit voltage of lithium ion batteries in a short time period". In: *Journal of Power Sources* 553 (Jan. 2023), p. 232295. DOI: `10.1016/j.jpowsour.2022.232295`.

[24] Matthieu Dubarry, Cyril Truchot, and Bor Yann Liaw. "Synthesize battery degradation modes via a diagnostic and prognostic model". In: *Journal of Power Sources* 219 (Dec. 2012), pp. 204–216. DOI: `10.1016/j.jpowsour.2012.07.016`.

[25] Sijia Yang, Caiping Zhang, Jiuchun Jiang, Weige Zhang, Yang Gao, and Linjing Zhang. "A voltage reconstruction model based on partial charging curve for state-of-health estimation of lithium-ion batteries". In: *Journal of Energy Storage* 35 (2021), p. 102271. ISSN: 2352-152X. DOI: `https://doi.org/10.1016/j.est.2021.102271`.

[26] Valentin Sulzer, Scott Marquis, Robert Timms, Martin Robinson, and S. Chapman. *Python Battery Mathematical Modelling (PyBaMM).* Feb. 2020. DOI: `10.1149/osf.io/5npy8`.

[27] Robert Timms, Scott G. Marquis, Valentin Sulzer, Colin P. Please, and S. Jonathan Chapman. "Asymptotic Reduction of a Lithium-Ion Pouch Cell Model". In: *SIAM Journal on Applied Mathematics* 81.3 (2021), pp. 765–788. DOI: `10.1137/20M1336898`.

[28] S.G. Marquis. *Long-term Degradation of Lithium-ion Batteries.* University of Oxford, 2020. URL: `https://books.google.se/books?id=4FMwzwEACAAJ`.

[29] Kieran O'Regan, Ferran Brosa Planella, W. Dhammika Widanage, and Emma Kendrick. "Thermal-electrochemical parameters of a high energy lithium-ion cylindrical battery". In: *Electrochimica Acta* 425 (2022), p. 140700. ISSN: 0013-4686. DOI: `https://doi.org/10.1016/j.electacta.2022.140700`.

[30] Madeleine Ecker, Thi Kim Dung Tran, Philipp Dechent, Stefan Käbitz, Alexander Warnecke, and Dirk Uwe Sauer. "Parameterization of a Physico-Chemical Model of a Lithium-Ion Battery: I. Determination of Parameters". In: *Journal of The Electrochemical Society* 162.9 (June 2015), A1836. DOI: `10.1149/2.0551509jes`.

[31] Madeleine Ecker, Stefan Käbitz, Izaro Laresgoiti, and Dirk Uwe Sauer. "Parameterization of a Physico-Chemical Model of a Lithium-Ion Battery: II. Model Validation". In: *Journal of The Electrochemical Society* 162.9 (June 2015), A1849. DOI: `10.1149/2.0541509jes`.

[32] Peyman Mohtat, Suhak Lee, Valentin Sulzer, Jason B. Siegel, and Anna G. Stefanopoulou. "Differential Expansion and Voltage Model for Li-ion Batter-

ies at Practical Charging Rates”. In: *Journal of The Electrochemical Society* 167.11 (July 2020), p. 110561. DOI: `10.1149/1945-7111/aba5d1`.

[33] E. Prada, D. Di Domenico, Y. Creff, J. Bernard, V. Sauvant-Moynot, and F. Huet. “A Simplified Electrochemical and Thermal Aging Model of LiFePO4-Graphite Li-ion Batteries: Power and Capacity Fade Simulations”. In: *Journal of The Electrochemical Society* 160.4 (Feb. 2013), A616. DOI: `10.1149/2.053304jes`.

[34] Limei Wang, Jingjing Sun, Yingfeng Cai, Yubo Lian, Mengjie Jin, Xiuliang Zhao, Ruochen Wang, Long Chen, and Jun Chen. “A novel OCV curve reconstruction and update method of lithium-ion batteries at different temperatures based on cloud data”. In: *Energy* 268 (2023), p. 126773. ISSN: 0360-5442. DOI: `https://doi.org/10.1016/j.energy.2023.126773`.

[35] Marc Doyle, Thomas F. Fuller, and John Newman. “Modeling of Galvanostatic Charge and Discharge of the Lithium/Polymer/Insertion Cell”. In: *Journal of The Electrochemical Society* 140.6 (June 1993), p. 1526. DOI: `10.1149/1.2221597`.

[36] Weilong Ai, Ludwig Kraft, Johannes Sturm, Andreas Jossen, and Billy Wu. “Electrochemical Thermal-Mechanical Modelling of Stress Inhomogeneity in Lithium-Ion Pouch Cells”. In: *Journal of The Electrochemical Society* 167.1 (Oct. 2019), p. 013512. DOI: `10.1149/2.0122001JES`.

[37] Rutooj Deshpande, Mark Verbrugge, Yang-Tse Cheng, John Wang, and Ping Liu. “Battery Cycle Life Prediction with Coupled Chemical Degradation and Fatigue Mechanics”. In: *Journal of the Electrochemical Society* 159 (Aug. 2012), A1730–A1738. DOI: `10.1149/2.049210jes`.

[38] Shuzhi Zhang, Xu Guo, Xiaoxin Dou, and Xiongwen Zhang. “A rapid online calculation method for state of health of lithium-ion battery based on coulomb counting method and differential voltage analysis”. In: *Journal of Power Sources* 479 (2020), p. 228740. ISSN: 0378-7753. DOI: `https://doi.org/10.1016/j.jpowsour.2020.228740`.

[39] “Thermal-electrochemical parameters of a high energy lithium-ion cylindrical battery”. In: *Electrochimica Acta* 425 (2022), p. 140700. ISSN: 0013-4686. DOI: `https://doi.org/10.1016/j.electacta.2022.140700`.

[40] Bin Pan, Dong Dong, Jionggeng Wang, Jianbo Nie, Shuangyu Liu, Yaohe Cao, and Yinzhu Jiang. “Aging mechanism diagnosis of lithium ion battery by open circuit voltage analysis”. In: *Electrochimica Acta* 362 (Dec. 2020), p. 137101. DOI: `10.1016/j.electacta.2020.137101`.

[41] Mohammad Farkhondeh and Charles Delacourt. “Mathematical Modeling of Commercial LiFePO 4 Electrodes Based on Variable Solid-State Diffusivity”. In: *Journal of The Electrochemical Society* 159 (Jan. 2012), pp. 177–192. DOI: `10.1149/2.073202jes]`.

[42] Juhyun Song and Martin Z. Bazant. “Effects of Nanoparticle Geometry and Size Distribution on Diffusion Impedance of Battery Electrodes”. In: *Journal of The Electrochemical Society* 160.1 (Nov. 2012), A15. DOI: `10.1149/2.023301jes`.

[43] Toby Kirk, Colin Please, and S. Chapman. “Physical Modelling of the Slow Voltage Relaxation Phenomenon in Lithium-Ion Batteries”. In: *Journal of The Electrochemical Society* 168 (June 2021). DOI: `10.1149/1945-7111/ac0bf7`.

DEPARTMENT OF SOME SUBJECT OR TECHNOLOGY
CHALMERS UNIVERSITY OF TECHNOLOGY
Gothenburg, Sweden
www.chalmers.se

CHALMERS
UNIVERSITY OF TECHNOLOGY